



# Strengths and limitations of in situ U–Pb titanite petrochronology in polymetamorphic rocks: An example from western Maine, USA

Jesse B. Walters<sup>1,2</sup>  | Alicia M. Cruz-Uribe<sup>2</sup>  | Won Joon Song<sup>2</sup> |  
Christopher Gerbi<sup>2</sup> | Kimberly Biela<sup>3</sup>

<sup>1</sup>Institut für Geowissenschaften, Goethe Universität, Frankfurt am Main, Germany

<sup>2</sup>School of Earth and Climate Sciences, University of Maine, Orono, Maine, USA

<sup>3</sup>Department of Anthropology and Geography, Colorado State University, Fort Collins, Colorado, USA

## Correspondence

Jesse B. Walters, Institut für Geowissenschaften, Goethe Universität, Frankfurt am Main 60438, Germany.  
Email: [thegeojesse@gmail.com](mailto:thegeojesse@gmail.com)

Handling Editor: Prof. Clare Warren

## Funding information

The University of Maine; US-DE Fulbright Kommission

## Abstract

Titanite is a potentially powerful U–Pb petrochronometer that may record metamorphism, metasomatism, and deformation. Titanite may also incorporate significant inherited Pb, which may lead to inaccurate and geologically ambiguous U–Pb dates if a proper correction is not or cannot be applied. Here, we present laser ablation inductively coupled plasma mass spectrometry (LA-ICP-MS)-derived titanite U–Pb dates and trace element concentrations for two banded calcisilicate gneisses from south-central Maine, USA (SSP18-1A and SSP18-1B). Single spot common Pb-corrected dates range from 400 to 280 Ma with  $\pm 12$ –20 Ma propagated 2SE. Titanite grains in sample SSP18-1B exhibit regular core-to-rim variations in texture, composition, and date. We identify four titanite populations: (1)  $397 \pm 5$  Ma (95% CL) low Y + HREE cores and mottled grains, (2)  $370 \pm 7$  Ma high Y + REE mantles and cores, (3)  $342 \pm 6$  Ma cores with high Y + REE and no Eu anomaly, and (4)  $295 \pm 6$  Ma LREE-depleted rims. We interpret the increase in titanite Y + HREE between ca. 397 and ca. 370 Ma to constrain the timing of diopside fracturing and recrystallization and amphibole breakdown. Apparent Zr-in-titanite temperatures ( $803 \pm 36^\circ\text{C}$  at  $0.5 \pm 0.2$  GPa) and increased  $X_{\text{Di}}$  suggest a thermal maximum at ca. 370 Ma. Population 3 domains dated to ca. 342 Ma exhibit no Eu anomaly and are observed only in compositional bands dominated by diopside (>80 vol%), suggesting limited equilibrium between titanite and plagioclase. Finally, low LREE and high U/Th in Population 4 titanite dates the formation of hydrous phases, such as allanite, during high  $X_{\text{H}_2\text{O}}$  fluid infiltration at ca. 295 Ma. In contrast to the well-defined date–composition–texture relationships observed for titanite from SSP18-1B, titanite grains from sample SSP18-1A exhibit complex zoning patterns and little correlation between texture, composition, and date. We hypothesize that the incorporation of variable amounts of radiogenic Pb from dissolved titanite into recrystallized domains resulted in mixed dates spanning 380–330 Ma.

This is an open access article under the terms of the [Creative Commons Attribution](https://creativecommons.org/licenses/by/4.0/) License, which permits use, distribution and reproduction in any medium, provided the original work is properly cited.

© 2022 The Authors. *Journal of Metamorphic Geology* published by John Wiley & Sons Ltd.

Although titanite may reliably record multiple phases of metamorphism, these data highlight the importance of considering U–Pb data along with chemical and textural data to screen for inherited radiogenic Pb.

#### KEYWORDS

calcsilicate rocks, common Pb, thermobarometry, titanite petrochronology, U–Pb geochronology

## 1 | INTRODUCTION

Titanite ( $\text{Ca}[\text{Ti,Al,Fe}^{3+}]\text{SiO}_4[\text{O,OH,F,Cl}]$ ) is a common accessory phase and regularly participates in reactions with major phases (see review in Kohn, 2017). Similar to zircon and monazite, the incorporation of U and a variety of trace elements (e.g., Zr, Nb, Sr, and Y + REE) make titanite a potentially useful petrochronometer (Frost et al., 2000; Kohn, 2017). In particular, Zr-in-titanite thermometry and TZARS (titanite with anorthite, clinozoisite, rutile, and quartz) barometry allow for the estimation of both pressures ( $P$ ) and temperatures ( $T$ ) of metamorphism (Hayden et al., 2008; Kapp et al., 2009). However, the reactivity of titanite with major phases and fluids during metamorphism presents both benefits and drawbacks. Titanite U–Pb dates have been interpreted to reflect a variety of processes, including neocrystallization and growth (Castelli & Rubatto, 2002; Cioffi et al., 2019; Corfu, 1996; Kohn & Corrie, 2011; Rapa et al., 2017; Scott & St-Onge, 1995; Spencer et al., 2013; Stearns et al., 2015, 2016; Storey, Smith, & Jeffries, 2007; Verts et al., 1996; Walters & Kohn, 2017), fluid-driven recrystallization or alteration (Cioffi et al., 2019; Corfu, 1996; Garber et al., 2017; Holder & Hacker, 2019; Marsh & Smye, 2017; Storey, Smith, & Jeffries, 2007), Pb volume diffusion and cooling (Cherniak, 1993; Kirkland et al., 2016; Mattinson, 1978; Mezger et al., 1991; Spear & Parish, 1996; Tucker et al., 1987), and deformation-induced recrystallization (Bonamici et al., 2015; Gordon et al., 2021; Papapavlou et al., 2017, 2018; Spencer et al., 2013; Timms et al., 2020). Additionally, disequilibrium between titanite and zircon (or quartz) may result in overestimated Zr-in-titanite temperatures (Cruz-Uribe et al., 2018; Cioffi et al., 2019; Johnson et al., 2020). Combined, these factors greatly complicate linking titanite textures, compositions, and U–Pb dates to metamorphic, metasomatic, and tectonic processes.

Historically, titanite U–Pb geochronometry was interpreted to date cooling, as opposed to peak metamorphism, in high-grade metamorphic terranes. Early studies of Pb diffusion rates in titanite proposed relatively low closure temperatures ( $T_c$ ) of 450–600°C based on natural samples (e.g., Gascoyne, 1986; Heaman & Parrish, 1991;

Mattinson, 1978; Mezger et al., 1993). Later, experimentally derived Pb in titanite diffusion rates determined by Cherniak (1993) suggested a  $T_c$  of 600°C for a 100  $\mu\text{m}$  titanite grain cooling at a rate of 10°C/Myr (Kohn, 2017). Variations in morphology, colour, and U–Pb ratios of titanite from contact aureoles were interpreted to reflect variable diffusive resetting of Pb isotope compositions (e.g., Mezger et al., 1991, 1993; Tucker et al., 1987). In contrast, studies by Corfu and Muir (1989), Corfu and Ayres (1991), Verts et al. (1996) and others suggested that variations in titanite U–Pb ratios may reflect multiple or protracted metamorphic and/or metasomatic events. A growing number of studies of natural titanite over the past decade suggest that volume diffusion rates of Pb are greatly overestimated (Gao et al., 2012; Garber et al., 2017; Hartnady et al., 2019; Holder & Hacker, 2019; Holder et al., 2019; Kohn & Corrie, 2011; Kohn, 2017; Smye et al., 2018; Spencer et al., 2013; Stearns et al., 2016; Walters & Kohn, 2017). Revised estimates for Pb diffusion coefficients range from  $1 \times 10^{-20}$  to  $1 \times 10^{-26}$  ( $\text{m}^2 \text{s}^{-1}$ ) (Holder et al., 2019; Kohn, 2017), equivalent to the experimentally derived diffusion rate for Sr in titanite (Cherniak, 1995). These data suggest that volume diffusion is unlikely to disturb U–Pb dates in titanite metamorphosed at temperatures <850°C at most metamorphic time scales.

In the absence of Pb diffusion, disturbance of titanite U–Pb is anticipated to occur through fluid- or deformation-induced recrystallization. Consequently, multigenerational titanite with both recrystallized and secondary domains is commonly observed (e.g., Castelli & Rubatto, 2002; Cioffi et al., 2019; Corfu, 1996; Corfu & Ayres, 1991; Corfu & Muir, 1989; Garber et al., 2017; Holder & Hacker, 2019; Johnson et al., 2020; Spencer et al., 2013; Storey, Smith, & Jeffries, 2007; Smith et al., 2009; Tucker et al., 2004; Verts et al., 1996). Recrystallized zones are typically patchy to lobate and often oriented along fractures and cleavage planes, consistent with interface-coupled dissolution–reprecipitation reactions (ICDR) (Bonamici et al., 2015; Garber et al., 2017; Holder & Hacker, 2019; Marsh & Smye, 2017; Walters & Kohn, 2017). During ICDR, minerals in disequilibrium with a fluid will dissolve until the

chemical potential of the solid assemblage and fluid phase is equal, followed by precipitation at the reaction front once the fluid has reached supersaturation (see review in Putnis, 2009). Alternatively, depolymerization of the precursor grain may form an intermediate amorphous phase which may then recrystallize (Konrad-Schmolke et al., 2018).

One of the pitfalls of titanite U–Pb geochronology is that significant Pb may be incorporated upon crystallization, and a correction for the initial common Pb composition is often required (see discussions in Storey et al., 2006; Kirkland et al., 2018; Bonamici & Blum, 2020). Isotopic homogenization of Pb during metamorphism is required to obtain accurate U–Pb ages (Romer, 2001); however, ICDR may lead to two- or three-component mixing, such that the initial  $^{207}\text{Pb}/^{206}\text{Pb}$  composition of the recrystallized domains is a mix of radiogenic Pb grown since the neogrowth of the titanite, radiogenic Pb that may have been inherited from a precursor mineral, and unradiogenic ‘common’ Pb incorporated during exchange with the bulk reactant assemblage. Inherited radiogenic Pb has been identified in both neocrystallized titanite grains replacing precursor high-U phases (Kirkland et al., 2017, 2018; Romer & Rötzler, 2003), such as rutile, and in titanite recrystallized by ICDR (Castelli & Rubatto, 2002). Inherited radiogenic Pb has been observed in allanite (Romer & Siegesmund, 2003). Even phases that typically incorporate little initial Pb, such as monazite, may inherit old radiogenic Pb during ICDR recrystallization (e.g., Seydoux-Guillaume et al., 2003; Weinberg et al., 2020). Thus, the degree to which titanite dates reflect the timing of recrystallization requires careful consideration.

Here, we present titanite textural observations coupled with in situ compositional and U–Pb isotopic data by electron probe microanalysis (EPMA) and laser ablation inductively coupled plasma mass spectrometry (LA-ICP-MS) for two calcsilicate gneisses from western Maine, USA. In one sample (SSP18-1B), titanite textures, major and trace element compositions, and U–Pb dates strongly correlate. Variations in major and trace element concentration between these populations are linked to different stages of high-temperature metamorphism, deformation, and fluid infiltration. In contrast, titanite analyses from a second sample (SSP18-1A) exhibit a decoupling of U–Pb dates from textures and compositions, indicative of inherited radiogenic Pb from precursor titanite domains. These two samples, collected at the same outcrop, illustrate both the strengths and weaknesses of U–Pb titanite petrochronology in poly-metamorphic terranes.

## 2 | GEOLOGIC SETTING

### 2.1 | Regional overview

The geology of central and western Maine is dominated by extensive metasedimentary sequences of the Central Maine Trough and Connecticut Valley–Gaspé Trough, which extend from Connecticut through Newfoundland (Figure 1a) (Hibbard et al., 2006). In the Late Silurian to Early Devonian, these sediments were deposited into extensional basins within the Ganderian margin following accretion to Laurentia (e.g., Rankin et al., 2007). These sediments were subsequently metamorphosed during the Acadian and Neocadian orogenies (425–380 Ma) (Hillenbrand & Williams, 2021; Robinson et al., 1998; van Staal et al., 2009), resulting in a state-wide metamorphic gradient spanning from greenschist facies rocks in northeastern Maine to a high-*T* migmatite terrane in southwestern Maine (Figure 1a) (see review in Guidotti, 1989). Temperatures calculated by Holdaway et al. (1997) at 310 MPa range up to 626–649°C in the highest-grade rocks. Holdaway et al. (1988) noted a N–S increase in pressure, ranging from  $235 \pm 25$  MPa for cordierite- and andalusite-bearing assemblages exposed in the northern lobe of the Lexington pluton to 400–500 MPa or possibly higher for the migmatitic rocks near Lewiston (Figure 1a). Higher *P* is supported by estimates of 550–640 MPa at 490–540°C for kyanite-bearing rocks exposed just south of the Sebago pluton (S, Figure 1a; Thomson & Guidotti, 1989).

The complex multiphase nature of the high-grade metamorphism has been debated over the past half century (e.g., Guidotti, 1970; Holdaway et al., 1988; Lux & Guidotti, 1985; Solar & Brown, 1999; Solar & Tomascak, 2016). Early tectono-metamorphic models for Maine describe high-grade regional metamorphism in the Acadian followed by pulses of contact metamorphism driven by pluton emplacement (see review in Guidotti, 1989). Indeed, the regional gradient is locally deflected around plutons (Figure 1a). Additionally, pluton and dike crystallization ages range from ca. 420 Ma for coastal plutons to 270–260 Ma for abundant gem pegmatites (Bradley et al., 2000, 2016). Dates of ca. 400 Ma throughout western and central Maine and New Hampshire are consistent with large scale high-*T* Acadian metamorphism (Gerbi & West, 2007; Moecher et al., 2021; Pyle et al., 2005; Sanislav, 2011; Smith & Barreiro, 1990; Solar et al., 1998; Wing et al., 2003). In the region surrounding the Mooslookmeguntic Igneous Complex (Figure 1a), Acadian metamorphic conditions are thought to have exceeded 450 MPa and 700°C in the migmatites, resulting in syntectonic melt generation,

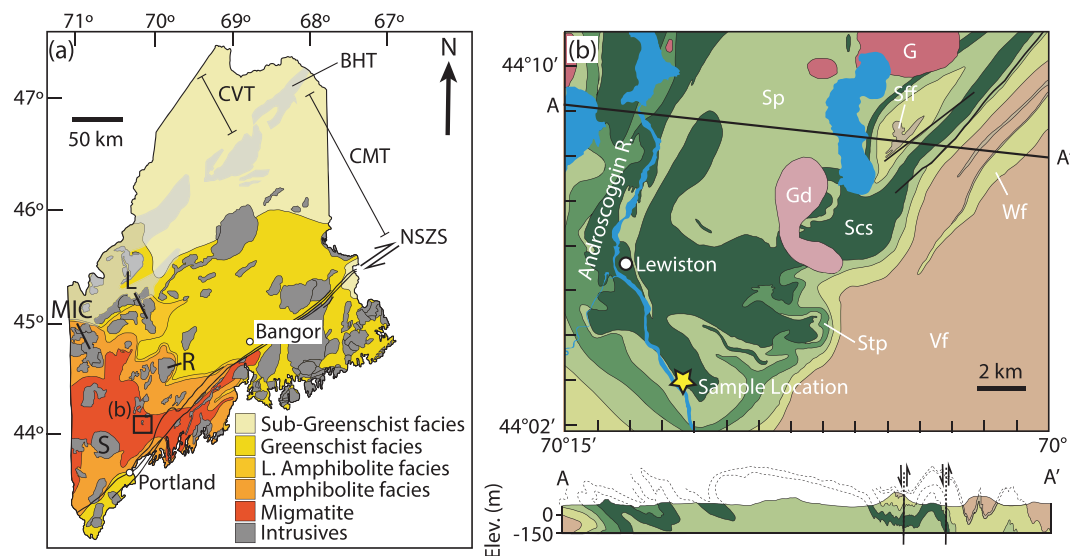


**FIGURE 1** (a) Map of Maine showing the distribution of metamorphic grades from sub-greenschist facies rocks in the north to migmatites in the southwest (after Guidotti, 1985; with updates from Solar & Brown, 1999). Major intrusions are highlighted, including the Lexington (L), Mooslookmeguntic (MIC), and Sebago (S) plutons. Also shown are the boundaries of the Connecticut Valley-Gaspé Trough (CVT) trough, Bronson Hill (BT) terrane, and Central Maine (CMT) trough. (b) Geologic map of the sample locality near Lewiston, Maine, and (c) cross-section from A to A' (after Hussey, 1983). Metasedimentary units include the Vassalboro (Vf), Waterville (Wf), Smalls Falls (Sff), and Sangerville formations. The latter is divided into pelitic (Sp), calcisilicate rich (Scs), and Taylor Pond (Stp) endmembers. Granite (G) and granodiorite (Gd) intrusions are observed north of the sample locality [Colour figure can be viewed at [wileyonlinelibrary.com](https://onlinelibrary.wiley.com/doi/10.1111/jmg.12657)]

percolative flow, and emplacement of granite magmas (Brown & Solar, 1999; Johnson et al., 2003).

The timing and conditions of high-grade metamorphism to the south in the vicinity of the Sebago pluton are more enigmatic. Emplacement of the Sebago 'batholith' was long considered responsible for much of the late high-grade metamorphism in western Maine (Figure 1a; see review in Guidotti, 1989). However, gravimetric and field mapping has revealed a much smaller Sebago pluton that sits at the core of an extensive migmatite terrane intruded by numerous smaller granitic bodies (Behn et al., 1998; Solar & Tomascak, 2016). Tomascak et al. (1996) reported a U–Pb monazite date of  $293 \pm 2$  Ma interpreted to reflect the crystallization age of the Sebago pluton. The crystallization ages of smaller granite and pegmatite bodies in the vicinity of the Sebago pluton range from 308 to 269 Ma (Solar & Tomascak, 2016; Tomascak et al., 1996). These ages contrast with a pooled zircon rim age of  $376 \pm 14$  Ma collected from three migmatite melanosomes (Tomascak & Solar, 2016), suggesting that the emplacement of the Sebago pluton is not responsible for partial melting in the surrounding region. Proposed mechanisms for metamorphism and melting in broader New England invoke the development of a thick crust and extended topographic high between ca. 400 and ca. 380 Ma (Hillenbrand et al., 2021), with thermal highs between ca. 380 and ca. 330 Ma that may have been generated by lithospheric delamination or slab break-off followed by

asthenospheric upwelling (e.g., Gibson et al., 2021; Moecher et al., 2021; Pyle et al., 2005; Robinson et al., 1998). The extent that regional, as opposed to contact, metamorphism is reflected in western Maine remains blurred by the murky temporal relationship between pluton emplacement, partial melting, and high-T metamorphism. Here we use titanite petrochronology to investigate the timing of high-temperature metamorphism in west-central Maine and distinguish between thermal sources.

## 2.2 | Sample locality

Three samples were collected in Lewiston, Maine, from the Sangerville formation, which in this area comprises three lithologic units: (1) migmatic paragneiss with the dominant assemblage  $Bt + Ms + Qtz + Pl \pm Sill \pm Grt \pm Kfs$  (Sp, Figures 1b and S1), (2) the Taylor Pond endmember paragneiss with the assemblage  $Bt + Qtz + Pl \pm Hbl$  and thin interbeds of calcisilicate (Stp), and (3) banded calcisilicate and metapsammitic gneiss (Scs, Figure S1c; Hussey, 1983). All abbreviations are after Whitney and Evans (2010). Two samples were collected from the calcareous bands (SSP18-1A and SSP18-1B), and a third was collected from a rare garnet-bearing horizon in the paragneiss (SS18-1D, Appendix S4). Samples were collected from blasted material at a quarry, and the exact spatial relationship between their original locations is not

known. All abbreviations are after Whitney and Evans (2010). Two larger intrusive bodies are observed to the northwest of the sample locality (Figure 1b). The larger two-mica granite pluton (G) exhibits sharp and discordant contacts with the metasediments and no obvious contact metamorphism (Hussey, 1983). Although the granite is undeformed, the fine- to medium-grained granodiorite body (Gd) is moderately to strongly foliated (Hussey, 1983). The outcrop includes at least two dike populations. The first population is parallel to the foliation of the migmatites and boudinaged (Figure S1a,b), whereas the second population crosscuts the foliation and exhibits sharp contacts with the host rock (Figure S1c,d). Pegmatite dikes are also common in the field area but are not observed in the sampled outcrop (Hussey, 1983).

### 3 | ANALYTICAL METHODS

Below, we detail the analytical methods for in situ titanite U–Pb and trace element analyses by LA-ICP-MS. Additional analytical methods for major and minor element analysis by EPMA, major mineral analysis by LA-ICP-MS, and electron backscatter diffraction (EBSD) analysis are detailed in Appendices S1–S3, respectively. Microprobe analyses are reported in Table S1.

#### 3.1 | Titanite U–Pb geochronology and trace element analysis

In situ titanite U–Pb and trace element analyses were conducted on polished thin sections by LA-ICP-MS in the University of Maine MAGIC (MicroAnalytical Geochemistry and Isotope Characterization) Lab over two separate sessions for samples SSP18-1A (Session 1) and SSP18-1B (Session 2). Titanite analysis locations are shown in Figures S4 to S6, and titanite LA-ICP-MS are shown in Table S2. Analytical conditions are summarized in

Table S3. Trace element and U–Pb data were collected using an ESI NWR193<sup>UC</sup> excimer laser ablation system coupled to an Agilent 8900 ICP-MS (see Table S3a). Plagioclase, alkali feldspar, and clinopyroxene in textural equilibrium were analysed for common <sup>207</sup>Pb/<sup>206</sup>Pb. Monitored isotopes and dwell times (ms) were <sup>29</sup>Si (5), <sup>43</sup>Ca (1), <sup>44</sup>Ca (1), <sup>49</sup>Ti (5), <sup>56</sup>Fe (1), <sup>88</sup>Sr (1), <sup>89</sup>Y (1), <sup>90</sup>Zr (5), <sup>93</sup>Nb (1), <sup>137</sup>Ba (1), <sup>139</sup>La (1), <sup>140</sup>Ce (1), <sup>141</sup>Pr (1), <sup>146</sup>Nd (1), <sup>147</sup>Sm (1), <sup>153</sup>Eu (1), <sup>157</sup>Gd (1), <sup>159</sup>Tb (1), <sup>163</sup>Dy (1), <sup>165</sup>Ho (1), <sup>166</sup>Er (1), <sup>169</sup>Tm (1), <sup>172</sup>Yb (1), <sup>175</sup>Lu (1), <sup>178</sup>Hf (1), <sup>181</sup>Ta (1), <sup>202</sup>Hg (40), <sup>204</sup>Pb (60), <sup>206</sup>Pb (40), <sup>207</sup>Pb (60), <sup>208</sup>Pb (30), <sup>232</sup>Th (10), <sup>235</sup>U (10), and <sup>238</sup>U (10). Silicon contents of 14.00 (±0.16, 2s) and 14.07 (±0.20, 2s) wt% determined by EPMA were used for internal standardization for SSP18-1A and SSP18-1B, respectively, to calculate trace element mass fractions. U–Pb dates were calculated using IsoplotR (Vermeesch, 2018), and pooled dates were determined using the maximum likelihood algorithm ('Model 1') of Ludwig (1998).

Analyses of unknowns were bracketed by those of titanite reference materials MKED1 (1518.87 ± 0.32 Ma; Spandler et al., 2016), BLR-1 (1047.1 ± 0.4 Ma; Aleinikoff et al., 2007), and McClure Mountain (523.26 ± 0.65 Ma; Schoene & Bowring, 2006), whose published U–Pb isotope ratios are given in Table S3b. Analyses of reference glasses were conducted for trace element determination (Table S3a). All titanite U–Pb isotope and trace element data for unknowns are reported in Table S2. Single spot dates are given with uncertainties reported as 2SE, which include random analytical uncertainties and reproducibility of the MKED1 reference material. In Table 1, full systematic uncertainties of pooled ages are also given following Horstwood et al. (2016) including ratio uncertainty of the MKED1 reference material (Table S3b), long-term variance of the validation material, uncertainties in the decay constant, and weighted uncertainties in the estimated common Pb composition (see below). We assume a 1% (2s) uncertainty on the long-term variance of the validation material, which is consistent with the magnitude of the <sup>238</sup>U/<sup>206</sup>Pb and <sup>207</sup>Pb/<sup>206</sup>Pb

TABLE 1 Summary of titanite date, trace element concentration, and Zr-in-titanite temperature for sample SSP18-1B

| Population | n  | Pooled lower-intercept dates <sup>a</sup> |                                    |      | Mean trace element concentrations (µg g <sup>-1</sup> ) |     |     | Zr-in-titanite temperature |                 |
|------------|----|---|------------------------------------|------|---|-----|-----|----------------------------|-----------------|
|            |    | Mean                                      | 95% CI <sub>sys</sub> <sup>b</sup> | MSWD | Y   | Zr  | Sr  | Wtd. mean                  | 2s <sup>c</sup> |
| 1          | 14 | 397                                       | 5                                  | 0.95 | 446   | 349 | 106 | 744                        | 44              |
| 2          | 12 | 370                                       | 7                                  | 1.80 | 895   | 935 | 76  | 803                        | 36              |
| 3          | 6  | 342                                       | 6                                  | 1.60 | 834   | 458 | 67  | 764                        | 1               |
| 4          | 26 | 295                                       | 6                                  | 2.50 | 1,510   | 368 | 53  | 749                        | 34              |

<sup>a</sup>Model 1 discordia (Vermeesch, 2018).

<sup>b</sup>Systematic uncertainties propagated (see text).

<sup>c</sup>Weighted standard deviation adjusted for overdispersion.

uncertainties for BLR-1 reported here (Table S3b). Pooled uncertainties are reported as 95% CI and are adjusted for overdispersion where the chi-squared  $p$ -value for the isochron fit is  $<0.05$  (Vermeesch, 2018). The systematic uncertainties result in a 0.1–0.3 Ma (95% CI) inflation in the uncertainties of the pooled ages.

Measured  $^{207}\text{Pb}/^{206}\text{Pb}$  ratios of clinopyroxene from SSP18-1A and SSP18-1B are  $0.9654 \pm 0.0393$  (2SE,  $n = 5$ ) and  $0.9554 \pm 0.0495$  ( $n = 10$ ), respectively. In contrast, feldspar  $^{207}\text{Pb}/^{206}\text{Pb}$  ratios are  $0.8730 \pm 0.0064$  ( $n = 15$ ) and  $0.8781 \pm 0.0061$  ( $n = 10$ ), respectively. Common Pb isotope analyses are reported in Table S3c. We estimate that 2–20% of the measured Pb is inherited ‘common’ unradiogenic Pb ( $f_{207}$ , Table S2a). As a result, dates that are uncorrected, corrected using the two-stage crustal evolution model of Stacey and Kramers (1975), and corrected with measured feldspar or pyroxene  $^{207}\text{Pb}/^{206}\text{Pb}$  ratios are equal within their respective uncertainties. Given the higher Pb concentrations in feldspar relative to clinopyroxene and smaller scatter, we calculated all dates using the feldspar Pb ratios. We discuss potential systematic inaccuracies introduced by our preferred method of common Pb correction in Section 8.2.

The measured dates, isotopic ratios, and trace element concentrations for secondary reference materials are consistent with published values. A summary of secondary reference U–Pb analyses is provided in Table S3b, with a full report of U–Pb and trace element analyses provided in Table S3d–g. The data in Table S3b suggest that ages are both precise and true relative to reference values within  $\pm 1$ –2% uncertainty (95% CI) (see Joint Committee for Guides in Metrology, 2012). We find that the trace element concentrations of NIST SRM612 and GSD-1G are within 3% and 14%, respectively, of reference values from Jochum, Weis, et al. (2011) and Jochum, Wilson, et al. (2011). Zr concentrations exhibit a larger bias (6% and 17%, respectively); however, MKED1 titanite was used as a reference material for Zr and the bias is likely due to matrix differences. Our trace element concentrations for BLR-1 are less consistent with published values (Table S3e). For example, our Zr concentrations are  $\sim 270 \mu\text{g g}^{-1}$  higher than those reported by Mazdab (2009). It is likely these differences represent trace element heterogeneity in the BLR-1 titanite.

### 3.2 | Titanite LA-ICP-MS mapping

Trace element maps of a titanite grain from SSP18-1A were also collected at the University of Maine. Maps were collected using fast washout tubing (1/8 in. bore diameter) and an ESI dual concentric injector ICP-MS torch. Analytical conditions consisted of a square  $\sim 7 \times 7 \mu\text{m}$

spot,  $88 \mu\text{m s}^{-1}$  raster rate,  $5 \text{ J cm}^{-2}$  beam energy density, 200 Hz repetition rate, and a He carrier gas flow rate of 1,100 ml/min. Monitored isotopes and dwell times (ms) were  $^{28}\text{Si}$  (1),  $^{49}\text{Ti}$  (1),  $^{89}\text{Y}$  (1),  $^{90}\text{Zr}$  (1),  $^{202}\text{Pb}$  (20),  $^{207}\text{Pb}$  (30), and  $^{238}\text{U}$  (10). The total ICP-MS duty cycle of 80 ms was synchronized to the laser pulse width following van Malderen et al. (2018) and van Elteren et al. (2019) to achieve pixel dimensions of  $\sim 7 \times 7 \mu\text{m}$ . Two lines of BLR titanite were rastered at the same conditions before and after the unknown titanite grain. The time-resolved signals were processed using the VizualAge UComPbine and Trace Elements data reduction schemes in Iolite (v4) using  $^{28}\text{Si}$  (14.2 wt%) as the internal standardization element for mass fraction calculations. Trace element maps were produced using CellSpace in Iolite4 (Paton et al., 2011; Paul et al., 2012; Woodhead et al., 2007). Final maps were reprocessed in XMapTools (Lanari et al., 2014, 2018; Raimondo et al., 2017).

## 4 | PETROGRAPHY AND MAJOR ELEMENT CHEMISTRY

Below, we describe the mineral assemblages, textures, and major element compositions for calcsilicate samples SSP18-1A and SSP18-1B and infer possible reactions. Additional petrographic description is given for the metapelitic sample (SSP18-1D) in Appendix S4, along with photomicrographs (Figure S2), garnet and biotite X-ray intensity maps (Figure S3), and garnet EPMA transects (Figure S4).

### 4.1 | Calcsilicate sample SSP18-1A

Sample SSP18-1A is a gneiss with alternating calcsilicate and metapsammitic bands comprising the peak mineral assemblages  $\text{Di} + \text{Kfs} + \text{Pl} + \text{Ttn} + \text{Ap}$  and  $\text{Bt} + \text{Pl}$ , respectively (Figure 2a–f). Minor and trace minerals in the calcsilicate band include pyrrhotite, calcite, and zircon, whereas only zircon is present in the psammitic bands. Plagioclase ( $\text{An}_{40-46}$ ), alkali feldspar, diopside, titanite, and apatite in the calcsilicate band exhibit a granular texture (Figure 2a,b), consistent with equilibrium. Major mineral compositions are summarized in Figure S5. Backscattered electron (BSE) images of alkali feldspar reveal intersecting linear high Ba zones (up to 1 wt%, Figure 2c). Diopside grains exhibit slight undulatory and patchy Fe–Mg zoning in BSE (Figure 2e). Calcite is rare ( $<< 1 \text{ vol}\%$ ), and quartz is not observed. The absence of quartz and rarity calcite in the peak assemblage is consistent with the prograde reaction proposed by Ferry (1976):

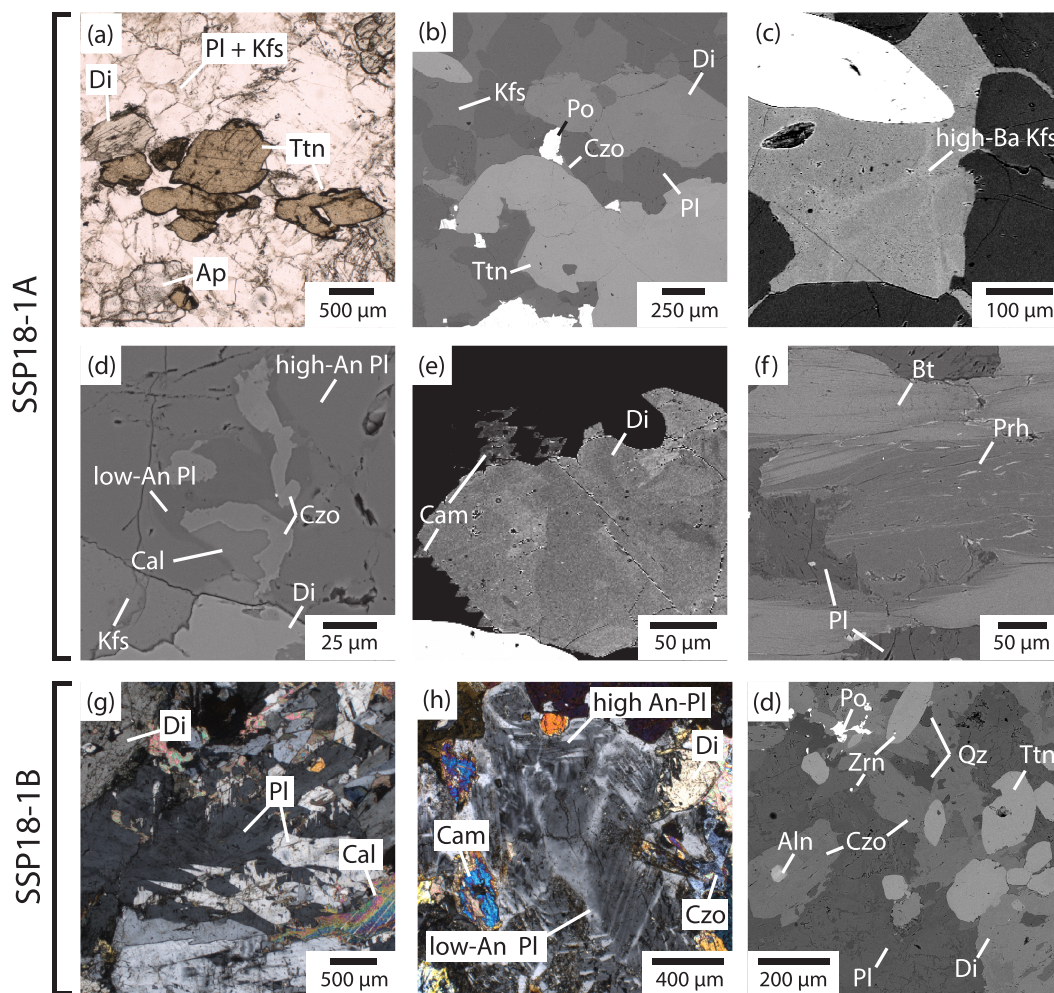
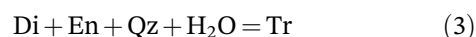
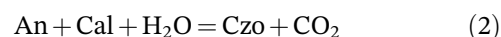


**FIGURE 2** Plane polarized light (a), cross-polarized light (g-h), and backscattered electron (BSE, b-f, d) images of minerals and textures in sample SSP18-1A and SSP18-1B. SSP18-1A: (a) large titanite grains adjacent to diopside, plagioclase, and alkali feldspar; (b) granular texture of plagioclase, alkali feldspar, and diopside adjacent to titanite, with small grains of clinozoisite and pyrrhotite; (c) high Ba BSE bright linear features observed in alkali feldspar; (d) a patch of intergrown clinozoisite, low-An Pl, and calcite adjacent to high-An plagioclase; (e) calcic amphibole and complex lobate zoning in diopside; and (f) prehnite replacing biotite in a metapsammitic band. SSP18-1B: (g) complex and sharply interlocking plagioclase grains are observed along with diopside and calcite, (h) oscillatory zones high-An plagioclase is cut by veins of low-An plagioclase, and (d) clinozoisite with allanite cores and rare quartz overprint earlier formed diopside, titanite, and plagioclase [Colour figure can be viewed at [wileyonlinelibrary.com](http://wileyonlinelibrary.com)]



While alkali feldspar is abundant (Figure S6), we observe no evidence of precursor K-bearing phases, such as biotite, in the calcsilicate band itself.

Retrograde minerals are observed only locally and make up <1–2 vol% or less of the sample. First, a second phase of An<sub>06</sub> plagioclase and clinozoisite replaces An<sub>40–46</sub> plagioclase and calcite (Figure 3d). Second, diopside grains are rimmed by calcic amphibole, which range in composition from Mg-hornblende to actinolite (Figures 2e and S6a,b). These textures are consistent with the following reactions in the CaO-MgO-Al<sub>2</sub>O<sub>3</sub>-SiO<sub>2</sub>-H<sub>2</sub>O-CO<sub>2</sub> system:

In particular, retrogression via Reactions 2 and 3 was likely limited by the rarity of calcite and quartz. In the psammitic bands, biotite grains are partially replaced by prehnite (Figure 2f). No clear Mg- or Fe-rich product phase is observed, and possible reactions require mobilization of these components into a fluid phase.

Titanite (~10 vol%) in the calcsilicate band occurs as large (<2.5 mm) grains. Misorientation maps show up to 10° of internal deformation that sweeps gradationally across grains, and larger misorientations occur associated

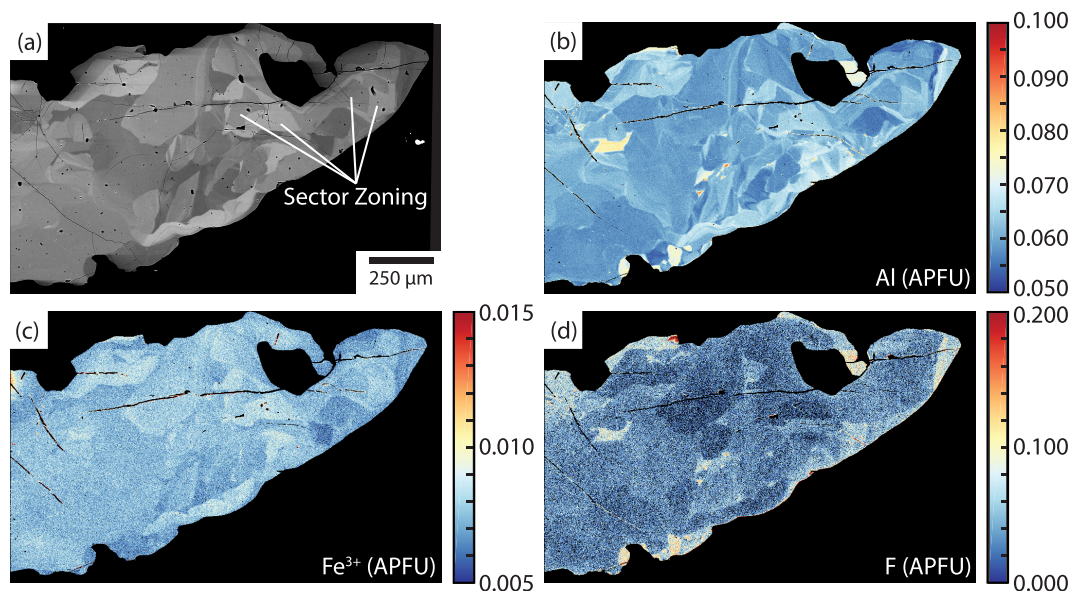
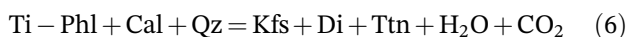
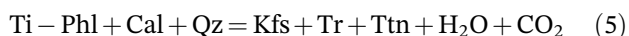
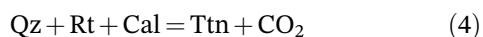
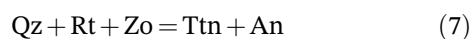


**FIGURE 3** (a) Back scattered electron image and quantitative maps of (b) Al, (c)  $\text{Fe}^{3+}$ , and (d) F concentrations in a titanite grain from SSP18-1A (grain 2, Figure S5). Concentrations are given in atoms per formula unit (APFU), and composition maps are produced by XMapTools (Lanari et al., 2014, 2018) [Colour figure can be viewed at [wileyonlinelibrary.com](http://wileyonlinelibrary.com)]

with fractures, grain boundaries, and twinning (Figures S7–S9). Misorientations are not correlated with compositional zoning in BSE (Figures S4 and S5). Titanite BSE images reveal a complex patchwork of overlapping zones with sharp to gradational boundaries (Figures S10 and S11). Sector zones, with their characteristic fir-tree shape, and cyclical zones are observed in some grains (Figure 3a). Titanite endmember fractions range from  $\text{Ttn}_{92}$  to  $\text{Ttn}_{94}$ , with considerable variation in Al,  $\text{Fe}^{3+}$ , and F shown in major element compositional maps (Figure 3b,c). Aluminium and  $\text{Fe}^{3+}$  are positively correlated within grain interiors, whereas BSE dark rims exhibit elevated Al + F and low  $\text{Fe}^{3+}$ . The observed zoning is thus consistent with the substitution  $(\text{Al}, \text{Fe})^{3+} + (\text{OH}, \text{F})^{-} = \text{Ti}^{3+} + \text{O}^{2-}$  (Kohn, 2017). Possible titanite forming reactions proposed by Frost et al. (2000) and Rapa et al. (2017) are as follows:



Additionally, if  $X_{\text{CO}_2}$  was sufficiently low during prograde metamorphism, the reaction



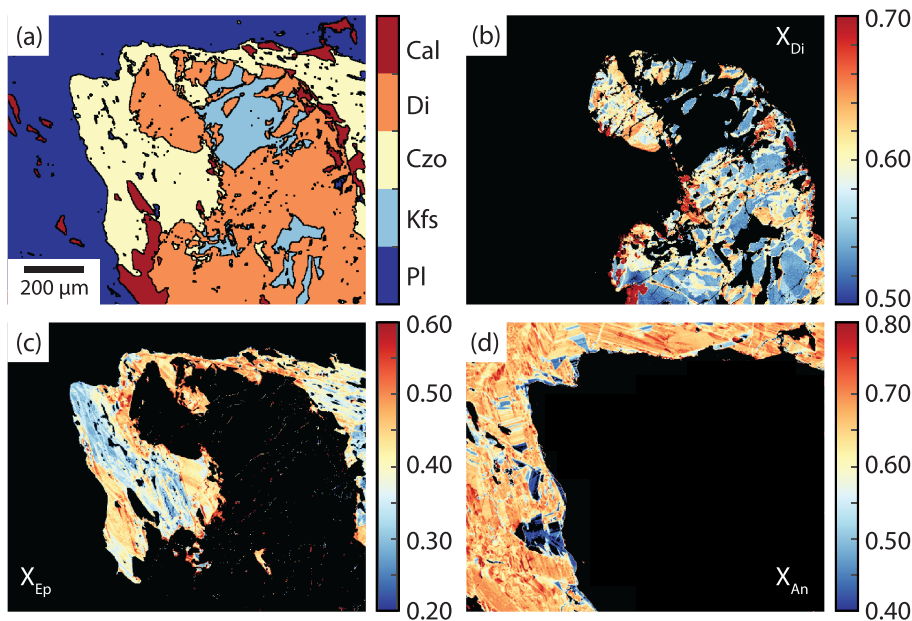
may have occurred. Other phases, such as amphibole and epidote group minerals, may contain significant Ti (Frei et al., 2004; Hawthorne et al., 2012), and their breakdown during prograde metamorphism may also promote titanite formation. However, the lack of prograde reaction textures and inclusions in titanite preclude clear petrographic identification of initial titanite forming reactions.

## 4.2 | Calcisilicate sample SSP18-1B

Sample SSP18-1B is a gneiss with alternating diopside- or plagioclase-rich bands (Figure S12). The peak assemblage  $\text{Di} + \text{Kfs} + \text{Pl} + \text{Cal} + \text{Ttn}$  is observed (Figures 2g–i and 4). Minor and trace phases include pyrrhotite and zircon. Calcite is rare, making up <10 vol% of plagioclase-rich bands. Plagioclase grains exhibit irregular interlocking grain boundaries with sharp spire-like intergrowths (Figure 2g) and more rarely cyclical zones (Figure 2h). These grains are often fractured and infilled by lower An plagioclase. Compositional maps and spot analyses reveal a range from  $\text{An}_{28}$  to  $\text{An}_{80}$  (Figures 4d and S5). Diopside grains exhibit intense fracturing and rehealing textures: Early diopside exhibits the composition  $\text{Di}_{53-54}$  which increases to  $\text{Di}_{58-70}$  in the later fracture-fill clinopyroxene (Figure 4b). Rare amphibole inclusions are observed in larger diopside grains, consistent with Reaction 1. Alkali feldspar is observed in fractured regions of diopside (Figure 4), suggesting the reaction

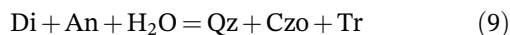


**FIGURE 4** (a) Phase map and quantitative compositional maps of the endmember fractions of (b) diopside ( $X_{Di}$ ) in clinopyroxene, (c) epidote ( $X_{Ep}$ ) in clinzoisite/epidote, and (d) anorthite ( $X_{An}$ ) in plagioclase in sample SSP18-1B. Maps are produced using the XMapTools software package (Lanari et al., 2014, 2018) [Colour figure can be viewed at [wileyonlinelibrary.com](http://wileyonlinelibrary.com)]



which may have occurred following the fracturing of the early diopside grains. However, no inclusions of biotite or relict matrix grains are observed.

Extensive amphibole and clinzoisite retrogression is observed in sample SS18-1B (Figure 2h). Amphibole compositions range from Mg-hornblende to actinolite from core to rim. Allanite occurs as cores in clinzoisite, suggesting LREE depletion from the reactive bulk composition as retrogression progressed (Figure 2i). Epidote compositions range from  $\text{Ep}_{29}$  to  $\text{Ep}_{60}$ , with higher Fe contents adjacent to diopside (Figure 4c). In some areas, clinzoisite is associated with quartz (Figure 2i), suggesting the hydration reaction



Elsewhere, clinzoisite has nucleated adjacent to calcite, consistent with the decarbonation-hydration Reaction 2 (Figure 4a).

Titanite grains (1–2 vol%) in sample SSP18-1B are relatively small (<800  $\mu\text{m}$ ) and lenticular in habit. Titanite grains are observed primarily in the matrix and as rare inclusions in diopside. The interiors of some rare grains exhibit oscillatory zoning or patchy cores, both with and without sectors (Figure S13). However, most grains exhibit regular core-to-rim zoning, with BSE dark cores observed in some grains, followed by a BSE bright mantle and a BSE dark rim (Figure S13). Many grains exhibit only bright cores and dark rims. Titanite compositions range from  $\text{Ttn}_{94}$  in the cores to  $\text{Ttn}_{87}$  in the rims.

## 5 | TRACE ELEMENT CHEMISTRY

Feldspar and diopside are the dominant peak metamorphic phases in our samples. Analyses of plagioclase reveal relatively high concentrations of Sr (160–1,684  $\mu\text{g g}^{-1}$ ), Ba (17.7–944  $\mu\text{g g}^{-1}$ ), Fe (46.8–1,476  $\mu\text{g g}^{-1}$ ), and Pb (0.291–23.9  $\mu\text{g g}^{-1}$ ). Plagioclase exhibits very low Eu concentrations (0.001–0.570  $\mu\text{g g}^{-1}$ ) but displays a positive Eu anomaly relative to Sm and Gd, which are below detection. Alkali feldspar in SSP18-1A exhibits elevated Ba (5,296–7,064  $\mu\text{g g}^{-1}$ ), Sr (790–1,054  $\mu\text{g g}^{-1}$ ), Pb (33.4–66.7  $\mu\text{g g}^{-1}$ ), and Fe (18.4–40.0  $\mu\text{g g}^{-1}$ ), with a positive Eu anomaly. Diopside grains have elevated Ti (9.5–212  $\mu\text{g g}^{-1}$ ) and Sr (0.86–95.6  $\mu\text{g g}^{-1}$ ), relative to other trace elements, and exhibit high Y + HREE relative to LREE. In Sample SSP18-1B, Ti, Y (+HREE), and Sr concentrations decrease between early fractured high  $X_{Di}$  and healed low  $X_{Di}$  diopside domains (Figures 4b and 5).

Texturally late amphibole and epidote group minerals were also analysed. Amphibole compositions range between Ti (730–2,635  $\mu\text{g g}^{-1}$ ), Sr (8.84–37.8  $\mu\text{g g}^{-1}$ ), and Y (9.73–68.9  $\mu\text{g g}^{-1}$ ) and are depleted in LREE relative to HREE. Analyses of epidote and clinzoisite in Sample SSP18-1B reveal high Sr (690–1,595  $\mu\text{g g}^{-1}$ ) and Pb (30.8–138  $\mu\text{g g}^{-1}$ ) relative to other trace elements, elevated LREE relative to HREE, and a strong positive Eu anomaly ( $\text{Eu}/\text{Eu}^* = 2.1\text{--}9.7$ ). Analysis of an allanite core in epidote revealed high LREE (e.g., Ce  $\sim 37$  wt%), Th (2,024  $\mu\text{g g}^{-1}$ ), U (487  $\mu\text{g g}^{-1}$ ), and Ti (1,288  $\mu\text{g g}^{-1}$ ), with sharply decreasing abundance from the allanite core through the epidote mantle and rim.

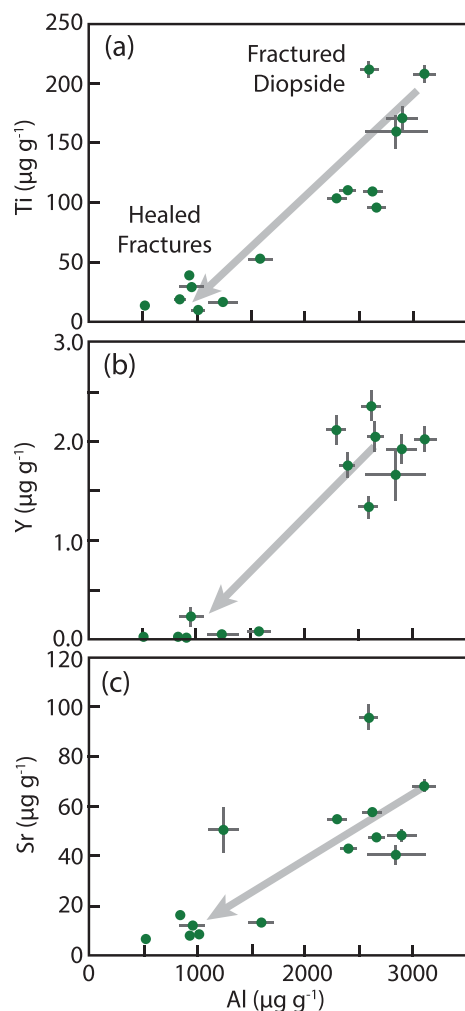


**FIGURE 5** Laser ablation inductively coupled mass spectrometry (LA-ICP-MS) analyses of diopside showing (a) Ti, (b) Y, and (c) Sr concentrations plotted relative to Al. Grey arrows indicate the trends from analyses of fractured low  $X_{\text{Di}}$  fragments and high  $X_{\text{Di}}$  recrystallized domains [Colour figure can be viewed at [wileyonlinelibrary.com](https://onlinelibrary.wiley.com/doi/10.1111/jmg.12657)]

Titanite grains exhibit a wide range of compositions. For example, Fe, Y, and Sr concentrations range from 1,227 to 2,526, 94 to 5,175, and 25.8 to 156  $\mu\text{g g}^{-1}$ , respectively (Figure 6). Rare earth element (REE) patterns vary considerably between and within samples. In SSP18-1B, titanite REE patterns range from steep negative MREE to HREE slope with high LREE to analyses with flat MREE to HREE and low LREE (Figure 7a). Some domains exhibit no Eu anomaly, whereas others exhibit a strong negative Eu anomaly. In contrast, sample SSP18-1A REE patterns range from relatively flat with strong negative Eu anomalies to MREE depleted patterns with positive Eu anomalies (Figure 7b). The correlation of these trace element patterns with age is discussed in Section 7.

## 6 | ZR-IN-TITANITE THERMOMETRY

Zr-in-titanite temperatures were calculated for samples SS18-1A and SS18-1B using the formulation of Thomas et al. (2010). Temperatures were calculated at 500 MPa with an associated 2s uncertainty of  $\pm 200$  MPa, corresponding to the 300–700 MPa range of possible pressures proposed for various stages of metamorphism in western Maine (Holdaway et al., 1988; Holdaway et al., 1997; Thomson & Guidotti, 1989; this study). The  $a_{\text{TiO}_2}$  of titanite-bearing rutile-absent metamorphic rocks is thought to be  $>0.5$  (Chambers & Kohn, 2012; Ghent & Stout, 1984); therefore, we assume a value of  $0.75 \pm 0.25$  (2s). Temperatures were also corrected for  $a_{\text{CaTiSiO}_5}$  using an ideal activity model and our measured  $X_{\text{Ttn}}$  and 2s uncertainties of  $0.93 \pm 0.01$  and  $0.91 \pm 0.05$  for samples SSP18-1A and SSP18-1B, respectively. All calculations assume  $a_{\text{SiO}_2}$  and  $a_{\text{ZrSiO}_4}$  of unity. Zircon grains are rare in the calcisilicate band of SSP18-1A, whereas zircon inclusions in titanite are common in SSP18-1B (Figures 2d and S13). Quartz is only observed in SSP18-1B associated with texturally late clinozoisite, and sample SSP18-1A is quartz-absent; therefore, the majority of our Zr-in-titanite temperatures for SSP18-1A and those calculated from interior zones in SSP18-1B are likely maxima. Temperatures are reported in Table S2c, and all temperatures are quoted in text are reported to the nearest 5°C.

Zr-in-titanite temperatures in samples SSP18-1A and SSP18-1B are 690–790°C and 690–830°C, respectively. Associated 2s uncertainties range from  $\pm 20^\circ\text{C}$  to  $22^\circ\text{C}$ . Hayden et al. (2008) argued that low Zr sector zones most closely approximate equilibrium, and their calibration was based on low Zr sectors when observed. We only observe a 6°C difference in calculated temperature between high and low Zr sectors in SSP18-1A, which is well within the calculated uncertainty.

In addition to Zr-in-titanite thermometry, we use the garnet-biotite thermometer of Ferry and Spear (1978) with the Berman (1990) garnet activity model and garnet-aluminosilicate-quartz-plagioclase (GASP) barometer using the calibration of Hodges and Crowley (1985) to estimate conditions of 630–700 MPa and 725–740°C for relatively unmodified garnet cores from metapelite sample SSP18-1D (for details see Appendix S5 and Figure S14). This estimate is consistent with the 690–830°C range calculated by Zr-in-titanite thermometry, sillimanite inclusions in garnet, and field observations, such as the distinct lack of thermal haloes around granite dikes and abundant leucosomes in the more pelitic portions of the sampled outcrop (Figure S1d).

**FIGURE 6** Laser ablation inductively coupled mass spectrometry (LA-ICP-MS) analyses of titanite showing concentrations of (a) Fe, (b) Sr, (c) Y, (d) Th/Pb, and (e) U/Th plotted relative to apparent age, as well as (f) Ce concentrations plotted against Sr. Data for sample SSP18-1B are colour coded by population: (1) yellow, (2) green, (3) blue, and (4) purple, whereas data for sample SSP18-1A are given in grey. Arrows indicate trends with time for sample SSP18-1B. Data plotted in f are labelled according to titanite location (diopside-rich or plagioclase-rich bands) and texture (BSE dark rims) [Colour figure can be viewed at [wileyonlinelibrary.com](http://wileyonlinelibrary.com)]

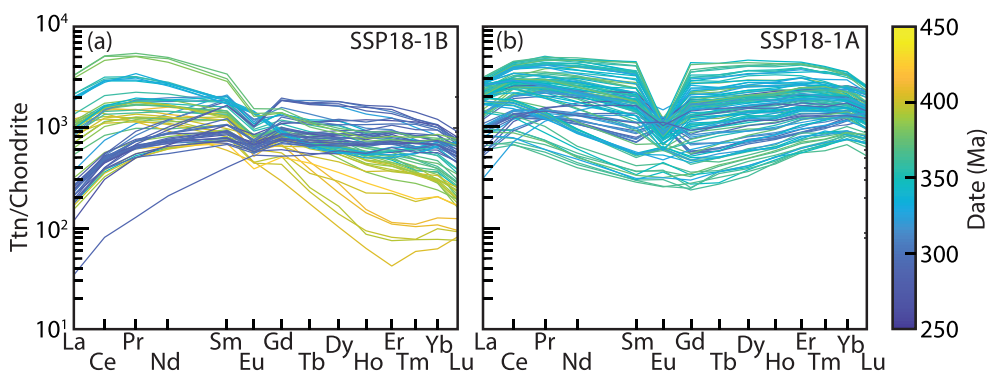
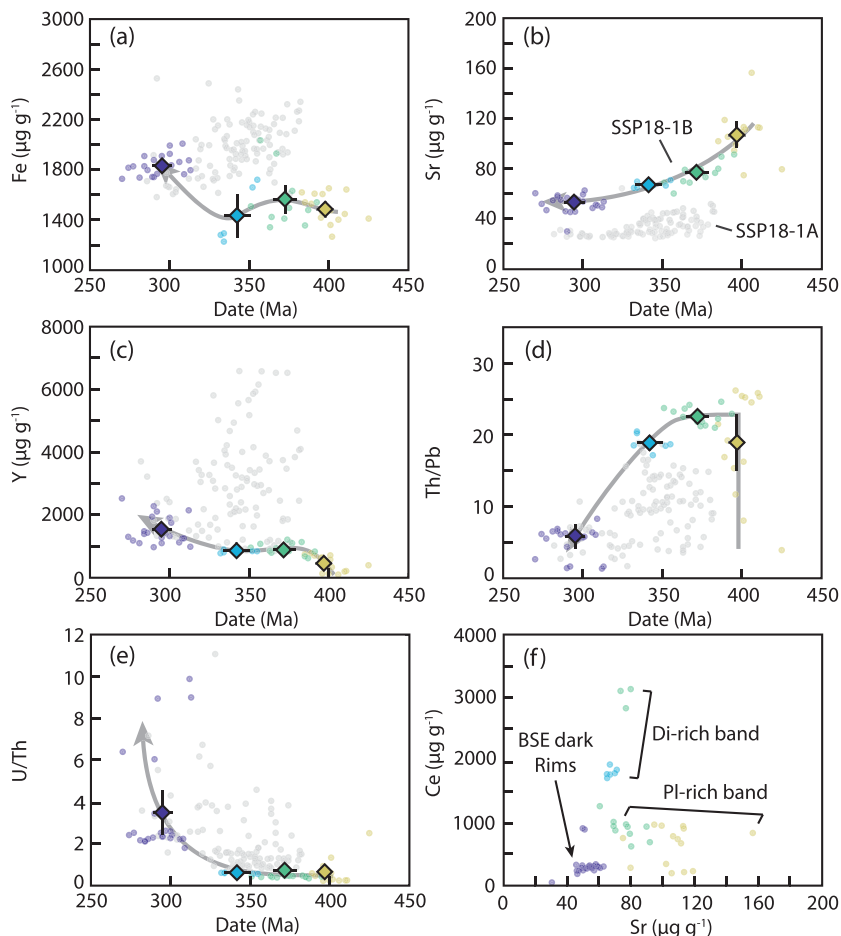


**FIGURE 7** Rare earth element diagrams of titanite laser ablation inductively coupled mass spectrometry (LA-ICP-MS) analyses for (a) samples SSP18-1B and (b) SSP18-1A. Concentrations on the y-axis are normalized relative to the CI chondrite values of Sun and McDonough (1989). The x-axis is scaled relative to ionic radius, and analyses are colour coded according to single spot common Pb-corrected dates [Colour figure can be viewed at [wileyonlinelibrary.com](http://wileyonlinelibrary.com)]

## 7 | TITANITE PETROCHRONOLOGY

Titanite single spot common Pb-corrected dates range from 400 to 280 Ma with 12–20 Ma propagated 2SE. In sample SSP18-1B, titanite displays distinctive trends in minor and trace element composition and REE pattern

with date (Figure 6). Zoning in BSE is largely concentric, with the oldest dates obtained from rare BSE dark cores and the youngest ages obtained from BSE dark rims (Figure S13). Analyses show an increase in Y and Fe through time, a decrease in Sr, variable Th/Pb, increasing U/Th, and a decoupling of Ce from Sr (Figure 6). Chondrite normalized REE patterns also reveal increasing

HREE through time, followed by a late depletion in LREE (Figure 7a). These trends correspond to distinct zones in BSE, revealing four texture-chemistry-date populations (Figure 8). First, BSE dark cores are dated to  $399 \pm 9$  ( $n = 4$ , mean standard weighted deviation (MSWD) = 0.83) and exhibit low Y + Fe + Zr concentrations and a steep negative MREE to HREE slope (Figures 6 and 7a). Two titanite grains (1 and 2, Figure S13a,b) show complicated internal zoning with mottled textures and occasional minor oscillations. These grains display dates, Y + Fe concentrations, and low HREE consistent with BSE dark core domains; however, some analyses of these regions give dates less than  $<380$  Ma which may indicate disturbance of the U–Pb system. If the oldest analyses of mottled zones are included with BSE dark zones, a pooled age of  $397 \pm 5$  ( $n = 14$ , MSWD = 0.95) is calculated for Population 1 (Table 1). BSE dark cores are surrounded by BSE bright mantles; however, in most grains, only BSE bright cores are observed. The BSE bright domains are divided into Populations 2 and 3. Population 2 domains give a pooled date of  $370 \pm 7$  ( $n = 12$ , MSWD = 1.80) and have elevated Y and Zr concentrations, a shallower MREE to HREE slope, and clear Eu anomaly (Table 1 and Figure 7a). Population 3 domains were observed in two grains with angular BSE bright cores and gives a pooled date of  $342 \pm 6$  ( $n = 6$ , MSWD = 1.60). Unlike Population 2, Population 3 domains exhibit lower Zr and Sr concentrations and display no Eu anomaly (Table 1 and Figure 7a). Finally, Population 4 BSE dark rim and mantle domains are dated to  $295 \pm 6$  ( $n = 26$ , MSWD = 2.50) and display high Y, low Zr + Sr, and a distinctive depletion in the LREE (Table 1 and Figure 7a).

In sample SSP18-1A, titanite grain interiors exhibit dates between 380 and 330 Ma and show significant scatter in trace element compositions and REE patterns (Figures 6 and 7), whereas young BSE dark rims ( $<330$  Ma) exhibit restricted compositions similar to those observed in SSP18-1B. Young BSE dark rims have lower Zr and give a pooled date of  $306 \pm 7$  Ma (MSWD = 3.50,  $n = 19$ ). The rim domains exhibit generally lower Fe, Y, Sr, and Th/Pb, and higher U/Th relative to older interior domains but do not display as strong of a LREE depletion as observed in SSP18-1A (Figures 6, 7, and 9). However, unlike SSP18-1B, no clear trends with date are observed within the interior zone analyses: These analyses produce a cloud of data in  $^{238}\text{U}/^{206}\text{Pb}$ – $^{207}\text{Pb}/^{206}\text{Pb}$  space (Figure 8b), and no correlation is observed between age and Y and Fe concentrations and REE pattern for dates within this range (Figures 6 and 7). A comparison of analysis location, zoning in BSE, and trace element concentrations reveals zones with similar composition and varying date and also

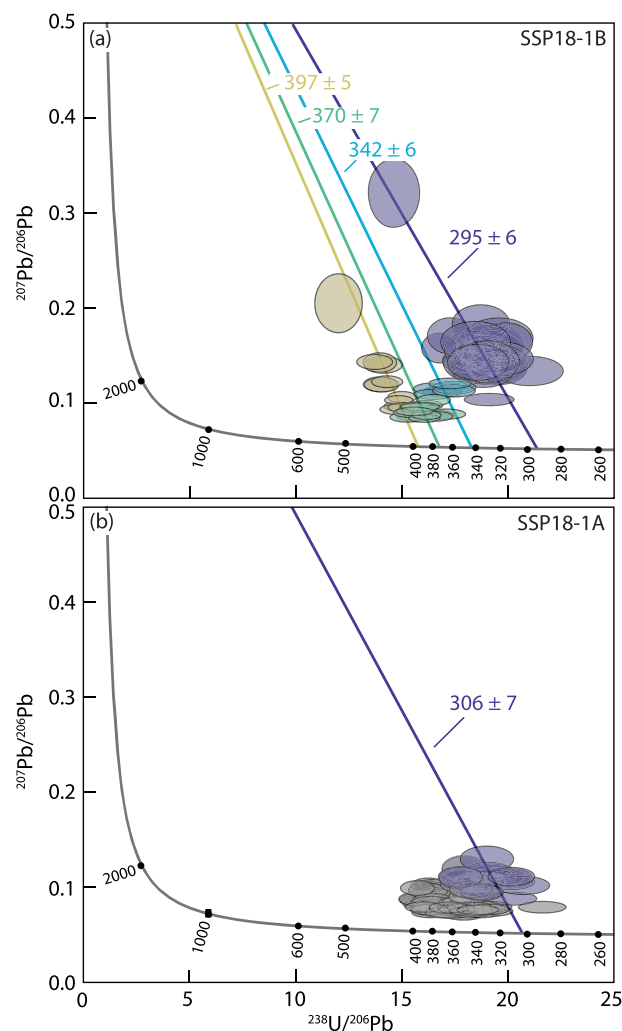
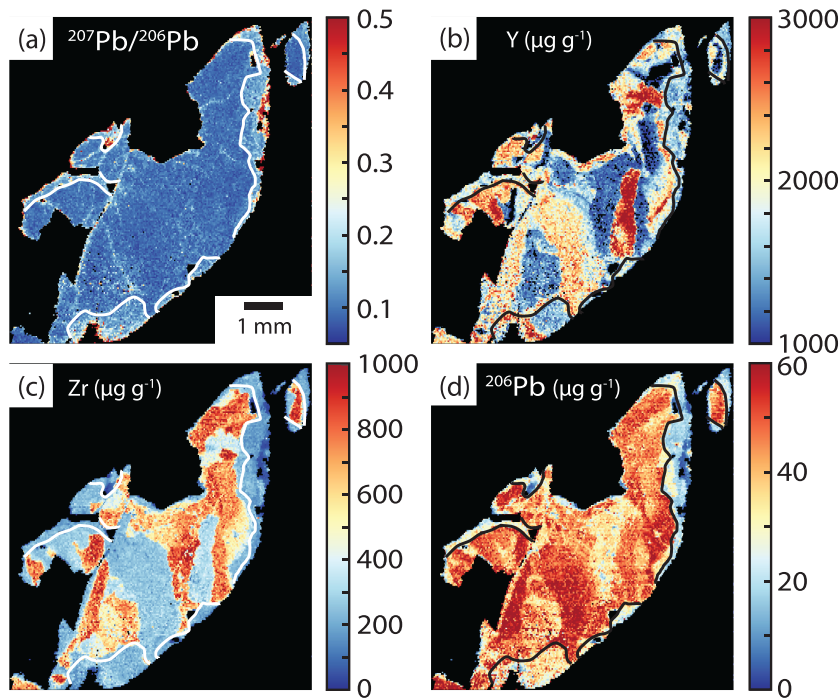


**FIGURE 8** Tera–Wassserburg diagrams for laser ablation inductively coupled mass spectrometry (LA-ICP-MS) analyses of titanite from samples (a) SSP18-1B and (b) SSP18-1A. Isochrons and pooled dates are shown with associated 95% CI as calculated in IsoplotR (Vermeesch, 2018). Isochrons and error ellipses are colour coded relative to populations 1 (yellow), 2 (green), 3 (blue), and 4 (purple) for sample SSP18-1B (a). An isochron for analyses of backscattered electron (BSE) dark rims in SSP18-1A is also shown in purple (b). Note that assignment to each isochron was based on texture (e.g., core, mantle, and rim) and composition; as a result, a single analysis of a titanite grain interior from SSP18-1A is not included in the rim regression despite occurring to the right of the isochron. Isochrons are anchored to  $^{207}\text{Pb}/^{206}\text{Pb}$  ratios of 0.0781 (a) and 0.0730 (b) measured in co-existing feldspar [Colour figure can be viewed at [wileyonlinelibrary.com](https://onlinelibrary.wiley.com/terms-and-conditions)]

crosscutting zones with distinct trace element compositions and overlapping dates (Figures S10 and S11). The latter case is demonstrated by LA-ICP-MS mapping of a titanite grain from SSP18-1A: Internal zones show large variation in Y and Zr concentrations at a nearly constant  $^{207}\text{Pb}/^{206}\text{Pb}$  of 0.07–0.10 (Figure 9). Rim domains consistently exhibit higher  $^{207}\text{Pb}/^{206}\text{Pb}$  ratios ( $>0.10$ ) relative to

**FIGURE 9** Laser ablation inductively coupled mass spectrometry (LA-ICP-MS) maps of (a)  $^{207}\text{Pb}/^{206}\text{Pb}$ , (b) Y, (c) Zr, and (d)  $^{206}\text{Pb}$  for a titanite grain from sample SSP18-1A. The white and black lines mark the boundary between young  $^{207}\text{Pb}/^{206}\text{Pb}$  enriched rims and older interior domains. Figures were reprocessed with the XMapTools software package (Lanari et al., 2014, 2018). Linear low  $^{207}\text{Pb}/^{206}\text{Pb}$  features in (a) are the result of Pb contamination in cracks [Colour figure can be viewed at [wileyonlinelibrary.com](https://onlinelibrary.wiley.com/doi/10.1111/jmg.12657)]



interior domains ( $<0.10$ ), suggesting a greater incorporation of unradiogenic initial Pb (Figure 9). Occasional sector zoning is observed in titanite grains from SSP18-1A (Figure 3a). Bright and dark sectors in BSE exhibit equivalent  $^{207}\text{Pb}/^{206}\text{Pb}$  ratios and U, Sr, and Nb concentrations, suggesting that these elements were not partitioned between sectors during crystallization. In contrast, Y and REE are enriched in BSE bright sectors by 150–200% and  $<50\%$ , respectively.

## 8 | DISCUSSION

### 8.1 | Linking titanite dates to metamorphic processes

Titanite grains in sample SSP18-1B reveal a 105 Myr history of metamorphism from ca. 400 to ca. 295 Ma. Titanite in this sample largely exhibit core-to-rim zoning in BSE, with a decrease in date between cores and rims (Figure S12), consistent with multiple stages of secondary overgrowth (e.g., Castelli & Rubatto, 2002). Beginning with the earliest stage, Population 1 BSE dark cores and mottled domains are dated to ca. 397 Ma and give a range of 690–785°C for maximum Zr-in-titanite temperatures. There is little textural evidence of this early metamorphic event. Initial neocrystallization of titanite may have formed by the breakdown of rutile or biotite (Reactions 4–6). No inclusions of biotite or rutile are observed in titanite or other phases, suggesting that these phases were not present following prograde metamorphism at

ca. 397 Ma. Amphibole and clinzoisite/epidote in calc-silicate rocks may also contain tens to thousands of  $\mu\text{g g}^{-1}$  of Ti (Table S4). The prograde breakdown of these phases may have also promoted Population 1 titanite crystallization. The wide range in Th/Pb ratios (5–25) observed in these domains (Figure 6d) does give some indication of possible reactions at ca. 397 Ma. Allanite will strongly fractionate Th from Pb, and the prograde breakdown of allanite may have increased the Th/Pb ratio of co-existing titanite (Figure 6d). Considerable variation in LREE concentrations is also observed in Population 1 domains, consistent with allanite breakdown (Figure 7a) (Johnson et al., 2020). Our explanation is consistent with rock-buffered fluid compositions anticipated for prograde metamorphism of calcsilicates: In a closed-system, prograde decarbonation reactions buffer the fluid from low  $X_{\text{CO}_2}$  conditions to higher  $X_{\text{CO}_2}$  conditions, resulting in the breakdown of early prograde epidote group minerals to form An-rich plagioclase (Figure 10a) (e.g., Ferry, 1976; Groppo et al., 2017; Rapa et al., 2017).

The transition between 397 Ma (Pop. 1) and 370 Ma (Pop. 2) domains is marked by a sharp increase in Y + HREE (Figures 6c and 7a) and a maximum Zr-in-titanite temperature of  $\sim 800^\circ\text{C}$  (Table 1). Garnet and amphibole may partition Y + HREE from titanite (Garber et al., 2017). Garnet is not observed as a prograde phase and only rarely occurs in the psammitic to pelitic bands in our field area; therefore, garnet breakdown at ca. 370 Ma is unlikely to have enriched titanite in these elements. Instead, amphibole is observed together with titanite as inclusions in diopside but does not occur in

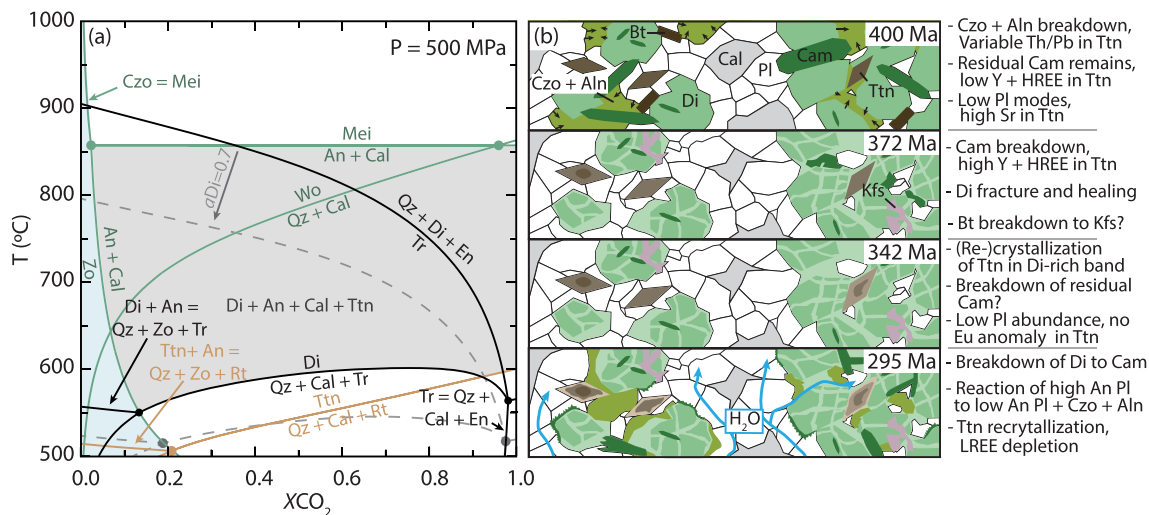


**FIGURE 10** (a) Petrogenetic T-X<sub>CO2</sub> grid calculated at 500 MPa for the CaO-Al<sub>2</sub>O<sub>3</sub>-SiO<sub>2</sub>-H<sub>2</sub>O-CO<sub>2</sub> (green), CaO-MgO-Al<sub>2</sub>O<sub>3</sub>-SiO<sub>2</sub>-H<sub>2</sub>O-CO<sub>2</sub> (black), and CaO-Al<sub>2</sub>O<sub>3</sub>-SiO<sub>2</sub>-TiO<sub>2</sub>-H<sub>2</sub>O-CO<sub>2</sub> (orange) systems calculated in *Perple\_X* (Connolly, 2005). Reactions involving MgO are also calculated with an activity of diopside (*a*<sub>Di</sub>) of 0.70. The grey field denotes the high-T moderate to high X<sub>CO2</sub> assemblage Di + An + Cal + Ttn, whereas the blue field denotes the stability field of Zo (or Czo). (b) A schematic diagram illustrating the reaction sequences inferred from mineral textures, compositions, and titanite trace element compositions between ca. 400 and ca. 295 Ma (see text for details) [Colour figure can be viewed at [wileyonlinelibrary.com](http://wileyonlinelibrary.com)]

the peak assemblage. We suggest that amphibole, rather than garnet, breakdown at ca. 370 Ma led to the increase in Y + HREE (Figure 10b). Diopside grains also reveal a protracted metamorphic history of an early low X<sub>Di</sub> phase followed by fracturing and recrystallization of diopside with higher X<sub>Di</sub> (Figure 4b). In addition to a decrease in Al and Fe between fractured and healed diopside, our analyses also reveal lower in Ti, Y, and Sr in healed domains (Figure 5). Given that titanite is the only high-T phase to partition Y + HREE over pyroxene in our rocks, mass balance requires recrystallization of fractured diopside formed at ca. 400 contributed to Y + HREE enrichment in titanite at ca. 370 Ma. Population 2 titanite likely formed through a combination of neocrystallization, as well as secondary overgrowth on Population 1 domains, driven by residual amphibole breakdown and diopside recrystallization (Figure 10b). Lower activities of diopside shift the diopside-in reactions to lower T (Figure 10a). The increase in X<sub>Di</sub> and high maximum Zr-in-titanite temperatures require that peak metamorphic conditions occurred at ca. 370 Ma.

Population 3 domains at ca. 342 Ma exhibit no Eu anomaly and lower maximum Zr-in-titanite temperature (~765°C) relative to Population 2 domains (Figure 7a and Table 1). Absolute Eu concentrations increase by ~30 µg g<sup>-1</sup> between ca. 370 and ca. 342 Ma, whereas Sm and Gd concentrations are constant. Plagioclase breakdown will release Eu relative to other REE. Plagioclase in SSP18-1B contains 1,098–1,282 µg g<sup>-1</sup> of Sr, and

plagioclase breakdown would release significant Sr in addition to Eu. Titanite Sr concentrations decrease through time across all domains (Figure 6b). Prograde metamorphism of calc-silicates at temperatures below scapolite stability produces increasing plagioclase modes at the expense of other Ca-bearing phases, such as calcite and clinozoisite (e.g., Ferry, 1976; Groppo et al., 2017; Walters & Kohn, 2017). We suggest that the decrease in titanite Sr concentrations with time represents increasing plagioclase modes. Therefore, plagioclase breakdown at ca. 342 Ma cannot account for the lack of the Eu anomaly in Population 3 titanite domains. Interestingly, Population 3 titanite was only observed in a diopside-rich (~80 vol.%) band (Figure 10b). Plagioclase incorporates Sr, but not LREE, whereas other phases, such as epidote group minerals, incorporate both Sr and LREE. Exchange between titanite and plagioclase will produce variable Sr, but LREE will remain unaffected. Population 2 and 3 titanite domains from the diopside-rich band exhibit variable Fe, low Sr, and high Ce, whereas Population 3 domains from the plagioclase-rich band exhibit a variable Sr concentrations and restricted Ce concentrations (Figure 6a,f). We suggest that poor intragrain mobility of trace elements between the diopside- and plagioclase-rich bands resulted in local equilibrium (thin section-scale disequilibrium). Additionally, local equilibria must have controlled titanite (re-)crystallization at ca. 342 Ma, as domains of this date are not observed in the plagioclase-rich bands (Figure 10b).

Finally, BSE dark Population 4 rims dated to ca. 295 Ma exhibit low Sr, Th/Pb, and LREE; high U/Th; and deep negative Eu anomalies (Figures 6 and 7a). We link these trace element characteristics to infiltration of a hydrous fluid during this final stage of titanite (re-)crystallization (Figure 10b). A decrease in  $X_{\text{CO}_2}$  to  $<0.10$  ( $X_{\text{H}_2\text{O}} > 0.90$ ) would stabilize clinozoisite over plagioclase and result in the breakdown of diopside to amphibole, both of which texturally overprint the earlier higher  $X_{\text{CO}_2}$  Di + Kfs + Pl + Cal assemblage in our samples. Clinozoisite-epidote Sr concentrations ( $771\text{--}1,595 \mu\text{g g}^{-1}$ ) overlap with those of plagioclase, consistent with plagioclase breakdown and the low Sr concentrations in Population 4 titanite. Additionally, clinozoisite-epidote grains exhibit positive Eu anomalies. Allanite, which is observed in some clinozoisite-epidote cores, contains elevated Th/Pb and LREE and low U/Th relative to titanite. Therefore, the low Sr, Th/Pb, and LREE; high U/Th; and deep negative Eu anomaly characteristic of Population 4 titanite may be entirely explained by exchange between titanite and epidote group minerals. Population 4 domains from both the plagioclase- and diopside-rich bands exhibit similar textures and compositions, suggesting a higher degree of trace element mobility at ca. 295 Ma. Cioffi et al. (2019), Garber et al. (2017), and Johnson et al. (2020) also observed titanite with low LREE and Sr in titanite from allanite-bearing rocks. Rims dated in sample SSP18-1A exhibit similar pooled date of  $306 \pm 7$  Ma ( $n = 19$ ,  $\text{MSWD} = 3.50$ ). In both samples, titanite rims are elevated in OH, F, and Al (Figure 3), consistent with a high  $X_{\text{H}_2\text{O}}$  fluid (Garber et al., 2017). Ferry (1976, 2016) observed a late influx of  $\text{H}_2\text{O}$ -rich fluids in rocks  $\sim 60$  km northeast of our field area, suggesting potentially widespread metasomatism and retrograde metamorphism at ca. 295 Ma.

## 8.2 | Decoupling of titanite U–Pb dates and trace element compositions

Lead-loss, U-mobility, and/or inheritance of unsupported radiogenic Pb can result in apparent ages that do not reflect the timing of metamorphism (e.g., Bonamici & Blum, 2020; Castelli & Rubatto, 2002; Garber et al., 2017; Kirkland et al., 2016, 2018; Romer & Rötzler, 2001, 2011; Romer & Siegesmund, 2003; Smye et al., 2018). As a result, U–Pb dates may decouple from major and trace element compositional zoning. Analyses of titanite grain interiors from sample SSP18-1A exhibit no clear trends in texture, major and trace element concentrations, and date between ca. 380 and ca. 320 Ma (Figure 6, 7b, and 9). Additionally, titanite grains interiors display equivalent dates between texturally overprinting zones, as well

as significant age variation within some chemically homogenous zones (Figures S10 and S11). Plotted in a Tera–Wasserburg diagram, the analyses of grain interiors in sample SSP18-1A form a sub-horizontal array with a narrow range (0.08 to 0.10) in  $^{207}\text{Pb}/^{206}\text{Pb}$  (Figure 8b). In contrast, rim analyses of titanite in SSP18-1A, dated to  $306 \pm 7$  Ma, exhibit more restricted trace element concentrations and are similar in composition and age to Population 4 rim analyses in Sample SSP18-1B. Based on these observations, we suggest that titanite dates for interior zones from sample SSP18-1A do not reflect the timing of (re-)crystallization.

The diffusion rate of Pb will differ from those of other trace elements with dissimilar size and charge; as a result, diffusive Pb-loss may decouple dates from trace element zoning patterns. Although experimental diffusion rates for Pb in titanite suggest a  $T_c$  of  $600^\circ\text{C}$  (Cherniak, 1993), natural data suggest Pb-loss by diffusion is unlikely to be efficient below  $850^\circ\text{C}$  (Hartnady et al., 2019; Holder et al., 2019; Kohn, 2017; Stearns et al., 2016; Walters & Kohn, 2017). Despite undergoing at least four metamorphic episodes, we observe no evidence that volume diffusion of Pb is responsible for the observed date variability. In SSP18-1B, core-to-rim variations in U–Pb date correspond closely to variations in texture and trace element chemistry, inconsistent with diffusive Pb-loss. Our dates for SSP18-1B also correlate well with known metamorphic and igneous events in the region, such as regional Acadian metamorphism at ca. 400 Ma and Neocadian metamorphism to the northwest at ca. 376 Ma (Sanislav, 2011; Smith & Barreiro, 1990; Solar et al., 1998; Tomascak & Solar, 2016). Lead-loss cannot explain the different U–Pb date–textural relationship between our two samples, which are from the same outcrop and experienced the same metamorphic histories. Additionally, the LA-ICP-MS Pb map of titanite from SSP18-1A reveals relatively sharp zoning (Figure 9d). Our data are therefore consistent with the reevaluated  $T_c$  for Pb in titanite.

Incorrect assumptions about the initial  $^{207}\text{Pb}/^{206}\text{Pb}$  may also result in a decoupling of titanite U–Pb dates from major and trace element patterns. Prograde, diagenetic, and detrital U-bearing phases, such as monazite, xenotime, allanite, and rutile, may break down during metamorphism (see discussions in Engi, 2017; Kohn, 2017) to release unsupported radiogenic Pb (e.g., Kirkland et al., 2018; Marsh & Smye, 2017; Romer & Siegesmund, 2003). As a result, the initial  $^{207}\text{Pb}/^{206}\text{Pb}$  ratio of a metamorphic mineral will represent a mixture of ‘common’ unradiogenic Pb and unsupported radiogenic Pb (Bonamici & Blum, 2020; Romer, 2001). Multiple analyses of one or more phases are commonly used to develop an isochron but assume that each aliquot received the

same initial  $^{207}\text{Pb}/^{206}\text{Pb}$  ratio. Metamorphic titanite  $^{238}\text{U}/^{206}\text{Pb}$  and  $^{207}\text{Pb}/^{206}\text{Pb}$  data often form linear arrays on Tera–Wasserburg diagrams, through which a linear regression constrains the initial  $^{207}\text{Pb}/^{206}\text{Pb}$  ratio (e.g., Bonamici & Blum, 2020; Kirkland et al., 2017, 2018; Marsh & Smye, 2017; Storey et al., 2006, 2007). However, multiple linear arrays with different initial  $^{207}\text{Pb}/^{206}\text{Pb}$  intercepts are sometimes observed, suggesting a variable contribution of unsupported radiogenic Pb (e.g., Bonamici & Blum, 2020; Romer & Rötzler, 2003). Correction of initial Pb by the isochron method is therefore only possible if linear arrays can be confidently discerned. Additionally, if radiogenic Pb released during the breakdown of U-bearing phases does not reach isotopic equilibrium with Pb in other phases then the  $^{207}\text{Pb}/^{206}\text{Pb}$  ratio of low U/Pb phases cannot be used to determine the initial  $^{207}\text{Pb}/^{206}\text{Pb}$  ratio of titanite. Often, the  $^{207}\text{Pb}/^{206}\text{Pb}$  ratios measured on U-poor phases, such as plagioclase and alkali feldspar, fall within the value of initial  $^{207}\text{Pb}/^{206}\text{Pb}$  defined by regression through titanite U–Pb data (e.g., Johnson et al., 2020; Kohn & Corrie, 2011; Walters & Kohn, 2017). For Sample SSP18-1B, we observe that isochrons for pooled dates at ca. 397 and ca. 295 Ma (Populations 1 and 2, respectively) demonstrate good agreement with the  $^{207}\text{Pb}/^{206}\text{Pb}$  ratio measured on plagioclase (Figure 8a). In contrast, U–Pb data from sample SSP18-1A form a cloud on the Tera–Wasserburg diagram with a narrow  $^{207}\text{Pb}/^{206}\text{Pb}$  ratio (Figure 10b). No isochrons are discernable for analyses of grain interiors, consistent with a variably mixed initial  $^{207}\text{Pb}/^{206}\text{Pb}$  ratio (Bonamici & Blum, 2020). Precursor U-bearing accessory phases inherited from the protolith may result in such a pattern but are expected to produce dates  $>400$  Ma (depending on the fraction of Pb contributed by the precursor phases), which are not observed. The only precursor accessory phase we observe is zircon, which appears to have been unreactive during metamorphism (see Section 8.4). We cannot completely rule out that precursor phases may have contributed some unsupported radiogenic Pb during titanite (re-)crystallization in sample SSP18-1A; however, we suggest that this scenario is unlikely.

U-mobility represents a third mechanism for producing the sub-horizontal U–Pb array observed in titanite from SSP18-1A. U-loss would produce dates greater than the age of metamorphism, and dates  $>400$  Ma are not observed. U-gain from an external source would require  $f\text{O}_2$  conditions inconsistent with the stability of pyrrhotite in SSP18-1A (see discussion in Garber et al., 2020). Therefore, we suggest that U-mobility is unlikely to explain the U–Pb isotope ratios observed in SSP18-1A.

Instead, we suggest that partial incorporation of unsupported radiogenic Pb during ICDR reactions is responsible for the decoupling of titanite textures,

compositions, and dates in Sample SSP18-1A. During ICDR, dissolution of the reactant phase produces a thin interfacial boundary layer of fluid that is supersaturated with respect to product phases, which nucleate at the reaction front (Putnis, 2009). Porosity is generated if the volume of reprecipitated solid matter is less than the volume dissolved, allowing the reaction front to propagate through the crystal if porosity is maintained (Ruiz-Agudo et al., 2014). Porosity is reduced at high temperatures by textural equilibration, and if the product phase is structurally similar to the reactant, crystallographic continuity may be preserved (Ruiz-Agudo et al., 2014).

Titanite grains from SSP18-1A exhibit crosscutting, lobate, uneven, and fragmentary zones which are consistent with extensive ICDR (Figures 3 and 9; see review in Putnis, 2009). The lack of correlation between variations in titanite crystallographic orientation and chemical zoning is also consistent with ICDR (Figures S7–S9). Lead liberated during titanite dissolution may be partially scavenged from the fluid before isotopic equilibrium is achieved with the bulk rock. For example, titanite formed at 400 Ma with 5% to 20% common Pb may have recrystallized during subsequent metamorphic recrystallization at 340 or 300 Ma (Figure 11). The entire range of titanite U–Pb ratios in SSP18-1A may be explained by 50% or less retainment of Pb during ICDR. Similar to our study, Castelli and Rubatto (2002) found that the mixed-dates of complexly zoned metamorphic titanite from the Western Alps represented incomplete isotopic resetting during recrystallization. Inheritance of unsupported radiogenic Pb has also been observed in monazite. For example, Seydoux-Guillaume et al. (2003) observed a spread in monazite dates between initial growth at 2.5 Ga and recrystallization at 790 Ma, which they attributed unsupported Pb in recrystallized domains. Weinberg et al. (2020) found that monazite dates, spread over 50 Myr, were decoupled from chemical zonation and reflected inherited radiogenic Pb from older domains during ICDR reactions. Similarly, Romer and Siegesmund (2003) found evidence of unsupported radiogenic Pb in allanite. When taken together with our study, these data suggest that dates of phases sensitive to ICDR, such as monazite, allanite, and titanite, may lack geological meaning in polymetamorphic rocks and should be carefully screened prior to interpretation.

In contrast to SSP18-1A, titanite from SSP18-1B is dominated by regular core-to-rim zoning in composition and date that is consistent with titanite crystallization (Castelli & Rubatto, 2002). We suggest that neocrystallization and secondary growth of titanite, which requires reactions with low U/Pb major mineral phases to liberate Ca, Ti, Al, and Si, will form titanite with an initial Pb composition dominated by common



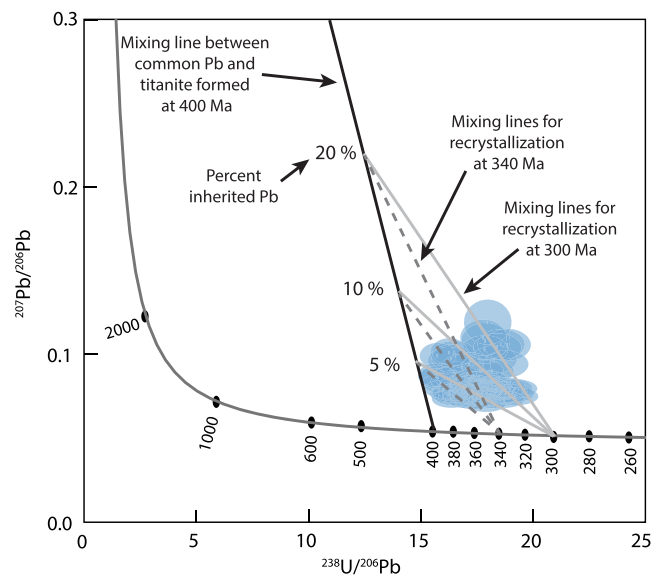


**FIGURE 11** Tera-Wasserburg diagram showing error ellipses for titanite interior zones (excluding rims) from SSP18-1A (blue). A mixing line between titanite formed at 400 Ma and a common Pb composition of 0.873 is shown in black. Mixing lines between the 400 Ma mixing line and theoretical titanite grains recrystallized at 340 (dark grey dashed lines) and 300 Ma (light grey solid lines) significantly overlap with the measured U–Pb data. Heterogeneous incorporation of 50% or less of unsupported radiogenic Pb from titanite crystallized at 400 Ma during recrystallization at 340 or 300 Ma would explain the narrow range of  $^{207}\text{Pb}/^{206}\text{Pb}$  ratios and lack of a linear arrays in the titanite U–Pb data [Colour figure can be viewed at [wileyonlinelibrary.com](http://wileyonlinelibrary.com)]

Pb. In contrast, recrystallization of titanite by ICDR may limit isotopic homogenization of Pb. Indeed, SSP18-1A and SSP18-1B appear to exhibit different bulk compositions and local environments, which may favour neocrystallization and secondary growth over ICDR: SSP18-1A is a banded gneiss with alternating alkali feldspar-bearing calcisilicate and metapsammitic bands, whereas SSP18-1B is a gneiss with alternating diopside- or plagioclase-rich bands and no alkali feldspar. Additionally, titanite exhibits a larger grain size and higher modal abundance in SSP18-1A ( $\leq 2.5$  mm,  $\sim 10$  vol%) relative to SSP18-1B ( $< 800$   $\mu\text{m}$ , 1–2 vol%), suggesting that a greater percentage of the bulk rock Pb budget is stored in titanite in SSP18-1A. These differences may have also played a role in the availability of radiogenic Pb relative to common Pb during titanite ICDR reactions.

### 8.3 | Common Pb uptake during crystallization

Titanite may incorporate significant common Pb upon crystallization (e.g., Bonamici & Blum, 2020; Kirkland

et al., 2018; Kohn, 2017; Romer & Rötzler, 2003; Storey et al., 2006, 2007). High ratios of common to radiogenic Pb require large extrapolations to concordia and result in U–Pb dates with high uncertainties. The initial U/Pb ratio inherited by titanite will be a function of the bulk rock U/Pb ratio and the relative partitioning of these elements between minerals during continuous and discontinuous metamorphic reactions (Romer, 2001).

Titanite in both our samples displays less than 20% inherited common  $^{207}\text{Pb}/^{206}\text{Pb}$  ( $f_{207}$ ) (calculated following Kirkland et al., 2016; 2018). In Figure 12, we plot  $f_{207}$  of titanite analyses from SSP18-1B as a function of date and Sr concentration. A decrease in  $f_{207}$  is observed between ca. 397 and ca. 370 Ma followed by an increase from ca. 342 to ca. 295 Ma (Figure 12a). Strontium concentrations in titanite are positively correlated with  $f_{207}$  at ca. 397 Ma, uncorrelated at ca. 372 Ma, and negatively correlated at ca. 295 Ma (Figure 12b). Plagioclase in SSP18-1B contains 20.5–23.9  $\mu\text{g g}^{-1}$  Pb, compared with 1.55–28.8  $\mu\text{g g}^{-1}$  measured in titanite (radiogenic + inherited Pb, Tables S2b and S4). Plagioclase is considerably more abundant (up to  $\sim 80$  vol% in plagioclase-rich bands) than titanite (1–2 vol%) and is therefore the largest Pb sink in SSP18-1B. The initial decrease in  $f_{207}$  and Sr corresponds to an increase in plagioclase modes between ca. 397 and ca. 370 Ma, whereas the elevated  $f_{207}$  at ca. 295 Ma corresponds to An-rich plagioclase breakdown (Figures 10b and 12). We suggest that the presence of phases that fractionate Pb from U, such as An-rich plagioclase and alkali feldspar, is a key factor contributing to low common Pb and may lead to both more precise and accurate titanite U–Pb ages.

### 8.4 | P–T conditions of retrogression and Zr-in-titanite disequilibrium

Population 4 titanite rim domains dated to ca. 295 Ma in sample SSP18-1B give Zr-in-titanite temperatures of  $\sim 750^\circ\text{C}$ . Titanite rims are associated with the retrograde assemblage amphibole, clinozoisite/epidote, allanite, albitic plagioclase, and quartz. The presence of zircon and retrograde quartz suggests that assumptions of unity for  $a_{\text{ZrSiO}_4}$  and  $a_{\text{SiO}_2}$  are reasonable for Population 4 Zr-in-titanite temperatures. The  $T$  estimate of  $750^\circ\text{C}$  is inconsistent with the retrograde assemblage in the calcisilicates. The reaction of diopside and anorthite to quartz, clinozoisite, and tremolite (Reaction 9) observed in SSP18-1B is expected to occur at  $\leq 550^\circ\text{C}$  at 500 MPa (Figure 10a). Additionally, attempts to calculate pressures using the TZARS barometer of Kapp et al. (2009) at  $750^\circ\text{C}$  produced unrealistically high pressures of

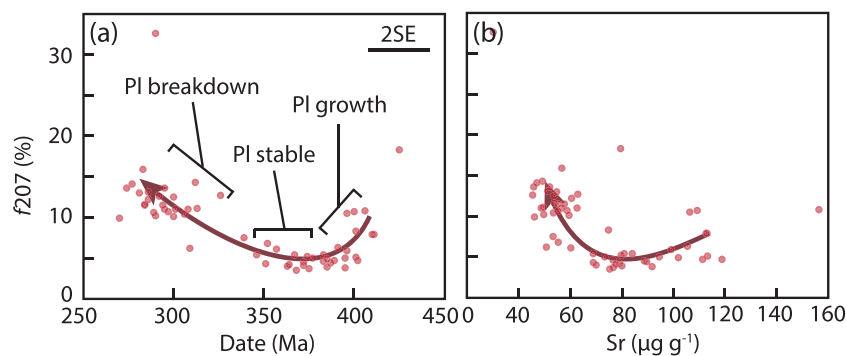


**FIGURE 12** Percent of common Pb ( $f_{207}$ ) in titanite plotted relative to (a) date and (b) Sr concentration. The average 2SE uncertainty of single spot dates (black scale bar) and trends with time (red arrow) is shown. In (a), plagioclase shows a trend of decreasing  $f_{207}$  attributed to plagioclase growth, followed by an increase in  $f_{207}$  corresponding to hydration, An-rich plagioclase breakdown and the formation of epidote group minerals. In (b), Sr concentrations roughly mirror the trend with date, showing correlation between  $f_{207}$  and Sr during the early and final stages of metamorphism [Colour figure can be viewed at [wileyonlinelibrary.com](http://wileyonlinelibrary.com)]

>1.0 GPa, whereas more reasonable pressures of 600 MPa were calculated for 500°C.

The Zr-in-titanite temperatures are also inconsistent with retrograde assemblages of metapelite and metapsammite rocks from the sampled outcrop. At 500 MPa, vapour-present muscovite-dehydration melting occurs at temperatures above ~650°C (Figure S14). Sillimanite is observed in garnet inclusions in metapelite sample SSP18-1D, and no sillimanite is observed in the matrix; in contrast, muscovite is abundant in the matrix but absent from inclusions. Rehydration of metapelites below the wet-solidus will produce muscovite at the expense of sillimanite (the reverse of the muscovite-dehydration reaction). Prehnite is observed to replace biotite in metapsammitic bands in Sample SSP18-1A. These textures require relatively low  $T$  retrogression and hydration of the metapelite and metapsammite rocks and suggest a shared history of fluid infiltration with the calcisilicate bands at ca. 295 Ma. Studies by Cioffi et al. (2019), Holder and Hacker (2019), and Johnson et al. (2020) suggested limited equilibrium between titanite and zircon, resulting in the overestimation of Zr-in-titanite temperatures by up to 150°C relative to temperatures calculated from other techniques. Here we also suggest that quartz and/or zircon cannot be in equilibrium with titanite at ca. 295 Ma and suggest caution when applying the Zr-in-titanite thermometer (e.g., Cruz-Urbe et al., 2018).

## 8.5 | Implications for the tectono-metamorphic history of western Maine

The Acadian and Neocadian Orogenies (425–380 Ma) are the dominant tectono-metamorphic events in the northern Appalachian Mountains and correspond to the

collision of the Avalon terrane with the eastern margin of Laurentia (Hillenbrand & Williams, 2021; Robinson et al., 1998; van Staal et al., 2009). Based on stratigraphic constraints and intrusion ages, Bradley et al. (2000) and Hillenbrand and Williams (2021) suggested that the Acadian crustal-thickening front moved from coastal Maine into Québec between at ca. 425 and ca. 380 Ma. The northwestward migration of the deformation front is consistent with ca. 400 Ma zircon and monazite ages observed throughout west-central Maine and New Hampshire (Gerbi & West, 2007; Gibson et al., 2021; Moecher et al., 2021; Pyle et al., 2005; Smith & Barreiro, 1990; Solar et al., 1998; Wing et al., 2003). We interpreted the pooled Population 1 titanite date of ca. 397 Ma to correspond to age of widespread regional Acadian metamorphism.

Studies of metamorphism in western Maine have long proposed that metamorphism in western Maine during the Neocadian (380–350 Ma) and Alleghenian (325–260) Ma orogenies (Robinson et al., 1998) was driven by pluton emplacement and contact heating, resulting in localized overprinting cycles of low- $P$  prograde and retrograde metamorphism (see review in Guidotti, 1989). The increase in  $X_{\text{Di}}$  between recrystallized and fractured diopside, breakdown of residual amphibole ( $\pm$  biotite), and higher maximum Zr-in-titanite  $T$  indicate that the highest thermal conditions experienced by our samples occurred at ca. 370 Ma (Figure 10). These data, in conjunction with the pooled ca. 376 Ma age of zircons from migmatites to the west of our field area (Tomascak & Solar, 2016), suggest that anatexis and deformation in this region occurred 20–30 Ma later than in the migmatites in the vicinity of the Mooselookmeguntic pluton (Figure 1a) (Brown & Solar, 1999; Johnson et al., 2003). Partial melting ceased prior to ca. 295 Ma,

suggesting no connection between anatexis and the emplacement of the Sebago pluton. Instead, high-*T* metamorphism at ca. 370 Ma overlaps with the 380–330 Ma period of partial melting observed in New Hampshire, central Massachusetts, and central Connecticut (see compilation in Hillenbrand et al., 2021). Retrograde metamorphism at ca. 295 Ma corresponds to the age of the Sebago pluton (Tomascak et al., 1996), which may have been the source of the high  $X_{\text{H}_2\text{O}}$  fluids.

Neocadian and Alleghenian metamorphism in western Maine is thought largely to be post-deformational, following localization of deformation to the Norumbega Fault System by ca. 380 Ma (Gerbi & West, 2007; Hubbard et al., 1995; Ludman, 1998; West, 1999; West & Hubbard, 1997). Metapelitic rocks in our field area exhibit stretched leucosomes that are oriented parallel to boudinaged dikes (Figure S1a,b), which require that anatexis and dike emplacement was either pre-tectonic or syntectonic. A second generation of dikes is also observed, but these are undeformed and crosscut the foliation of the host gneisses (Figure S1c,d). Based on these relationships, we also suggest that deformation in west-central Maine continued even after the initiation of dextral shear on the Norumbega Fault System, requiring that at least some strain was partitioned further inland.

## 9 | CONCLUSIONS

Titanite is a highly reactive mineral that may record multiple generations of crystallization, growth, and dissolution–reprecipitation. In addition, the temperature-dependent incorporation of Zr and the slow diffusivity of Pb make titanite a potentially excellent petrochronometer. However, titanite may incorporate significant initial Pb, potentially resulting in inaccurate age determination. Here we demonstrate both the benefits and shortcomings of titanite chronometry. Our data for sample SSP18-1B reveal four phases of metamorphism spanning a period from ca. 397 to ca. 295 Ma. Most titanite grains in this sample exhibit systematic core-to-rim variations in trace element concentrations and U–Pb dates, consistent with neocrystallization and secondary overgrowth. Trace element concentrations and REE patterns reflect changing partitioning between titanite and other phases, revealing the breakdown of hydrous phases between ca. 397 and ca. 342 followed by an influx of hydrous fluids at ca. 295 Ma. Metamorphism at ca. 397 Ma corresponds to the northwestward migration of the Acadian front, whereas the highest temperature conditions correspond to a period of metamorphism at ca. 372 Ma and are consistent with widespread partial melting observed throughout greater New England.

Retrogression at ca. 295 Ma may be related to hydrous fluids exsolved from the crystallizing Sebago pluton to the SW of our field area. In contrast, titanite from a second sample (SSP18-1A) exhibits little correlation between trace element concentrations, REE patterns, texture, and date. We suggest that date–composition decoupling is caused by the incorporation of variable amounts of unsupported radiogenic Pb in recrystallized domains, resulting in mixed geologically-meaningless ages. We suggest that titanite may reliably record multiple phases of metamorphism; however, U–Pb dates should be coupled with chemical and textural characterization to screen for unsupported radiogenic Pb in recrystallized domains.

## ACKNOWLEDGEMENTS

We thank M. Yates for assistance with EPMA analyses and H.L. Brooks and J. Stone for assistance with LA-ICP-MS analyses. Additionally, we thank J. Garber, M.J. Kohn, H. Marschall, W. Müller, and M. Konrad-Schmolke for fruitful discussions of these data. J. Ferry is thanked for suggesting calcisilicate sampling locations in Maine. We also thank C. Warren for editorial handling, N. Roberts and J. Darling for their comprehensive reviews, and I.W. Hillenbrand for an unofficial review of our preprint. JBW acknowledges support of fellowships from the US-DE Fulbright Kommission and the University of Maine.

## ORCID

Jesse B. Walters  <https://orcid.org/0000-0002-1275-8826>

Alicia M. Cruz-Uribe  <https://orcid.org/0000-0001-7270-0573>

## REFERENCES

- Aleinikoff, J. N., Wintsch, R. P., Tollo, R. P., Unruh, D. M., Fanning, C. J., & Schmitz, M. D. (2007). Ages and origins of rocks of the Killingworth dome, south-central Connecticut: Implications for the tectonic evolution of southern New England. *American Journal of Science*, 307, 63–118.
- Behn, M. D., Eusden, J. D., & Notte, J. A. II (1998). A three-dimensional gravity model of the southern contact of the Sebago pluton, Maine. *Canadian Journal of Earth Sciences*, 35, 649–656.
- Berman, R. G. (1990). Mixing properties of Ca-Mg-Fe-Mn garnets. *American Mineralogist*, 75, 328–344.
- Bonamici, C. E., & Blum, T. B. (2020). Reconsidering initial Pb in titanite in the context of in situ dating. *American Mineralogist*, 105(11), 1672–1685. <https://doi.org/10.2138/am-2020-7274>
- Bonamici, C. E., Fanning, C. M., Kozdon, R., Fournelle, J. H., & Valley, J. W. (2015). Combined oxygen-isotope and U–Pb zoning studies of titanite: New criteria for age preservation. *Chemical Geology*, 398, 70–84.
- Bradley, D., Shea, E., Buchwaldt, R., Bowring, S., Benowitz, J., O'Sullivan, P., & McCauley, A. (2016). Geochronology and

- tectonic context of lithium-cesium-tantalum pegmatites in the Appalachians. *Canadian Mineralogist*, *54*, 945–969.
- Bradley, D. C., Tucker, R. D., Lux, D. R., Harris, A. G., & McGregor, C. (2000). Migration of the Acadian orogen and foreland basin across the northern Appalachians of Maine and adjacent areas. *U.S. Geological Survey Professional Paper*, *1624*, 1–45.
- Brown, M., & Solar, G. S. (1999). The mechanism of ascent and emplacement of granite magma during transpression: A syn-tectonic granite paradigm. *Tectonophysics*, *312*, 1–33.
- Castelli, D., & Rubatto, D. (2002). Stability of Al- and F-rich titanite in metacarbonate: Petrologic and isotopic constraints from a polymetamorphic eclogite marble of the internal Sesia zone (Western Alps). *Contributions to Mineralogy and Petrology*, *142*, 627–639.
- Chambers, J. A., & Kohn, M. J. (2012). Titanium in muscovite, biotite, and hornblende: Modeling, thermometry, and rutile activities of metapelites and amphibolites. *American Mineralogist*, *97*, 543–555.
- Cherniak, D. J. (1993). Lead diffusion in titanite and preliminary results on the effects of radiation damage on Pb transport. *Chemical Geology*, *110*, 177–194.
- Cherniak, D. J. (1995). Sr and Nd diffusion in titanite. *Chemical Geology*, *125*, 219–232.
- Cioffi, C. R., da Costa Campos Neto, M., Möller, A., & Rocha, B. C. (2019). Titanite petrochronology of the southern Brasília Orogen basement: Effects of retrograde net-transfer reactions on titanite trace element compositions. *Lithos*, *344–345*, 393–408.
- Connolly, J. A. D. (2005). Computation of phase equilibria by linear programming: A tool for geodynamic modelling and its application to subduction zone decarbonation. *Earth and Planetary Science Letters*, *236*, 524–541.
- Corfu, F. (1996). Multistage zircon and titanite growth and inheritance in an Archean gneiss complex, Winnipeg River sub-province, Ontario. *Earth and Planetary Science Letters*, *141*, 175–186.
- Corfu, F., & Ayres, L. D. (1991). Unscrambling the stratigraphy of an Archean greenstone belt; a U–Pb geochronological study of the Favourable Lake belt, northwestern Ontario, Canada. *Precambrian Research*, *50*(3–4), 201–220. [https://doi.org/10.1016/0301-9268\(91\)90021-2](https://doi.org/10.1016/0301-9268(91)90021-2)
- Corfu, F., & Muir, T. L. (1989). The Hemlo-Heron Bay greenstone belt and Hemlo Au–Mo deposit, Superior Province, Ontario, Canada 2. Timing of metamorphism, alteration and Au mineralization from titanite, rutile, and monazite U–Pb geochronology. *Chemical Geology: Isotope Geoscience Section*, *79*(3), 201–223. [https://doi.org/10.1016/0168-9622\(89\)90030-4](https://doi.org/10.1016/0168-9622(89)90030-4)
- Cruz-Uribe, A. M., Feineman, M. D., Zack, T., & Jacob, D. E. (2018). Assessing trace element (dis)equilibrium and the application of single element thermometers in metamorphic rocks. *Lithos*, *314–315*, 1–15.
- van Elteren, J. T., Šelih, V. S., & Šala, M. (2019). Insights into the selection of 2D LA-ICP-MS (multi)elemental mapping conditions. *Journal of Analytical and Atomic Spectrometry*, *34*, 1919–1931.
- Engi, M. (2017). Petrochronology based on REE-minerals: Monazite, allanite, xenotime, apatite. *Reviews in Mineralogy and Geochemistry*, *83*, 365–418.
- Ferry, J. M. (1976). Metamorphism of calcareous sediments in the Waterville-Vassalboro area, south-central Maine: Mineral reactions and graphical analysis. *American Journal of Science*, *276*, 841–882.
- Ferry, J. M. (2016). Fluids in the crust during regional metamorphism: Forty years in the Waterville limestone. *American Mineralogist*, *101*, 500–517.
- Ferry, J. M., & Spear, F. S. (1978). Experimental calibration of the partitioning of Fe and Mg between biotite and garnet. *Contributions to Mineralogy and Petrology*, *66*, 113–117.
- Frei, D., Liebscher, A., Franz, G., & Dulski, P. (2004). Trace element geochemistry of epidote minerals. *Reviews in Mineralogy and Geochemistry*, *56*, 553–605.
- Frost, B. R., Chamberlain, K. R., & Schumacher, J. C. (2000). Sphehene (titanite): Phase relations and role as a geochronometer. *Chemical Geology*, *172*, 131–148.
- Gao, X.-Y., Zheng, Y.-F., Chen, Y.-X., & Guo, J. (2012). Geochemical and U–Pb age constraints on the occurrence of polygenetic titanites in UHP metagranite in the Dabie orogen. *Lithos*, *136–139*, 93–108. <https://doi.org/10.1016/j.lithos.2011.03.020>
- Garber, J. M., Hacker, B. R., Kylander-Clark, A. R. C., Stearns, M., & Seward, G. (2017). Controls on trace element uptake in metamorphic titanite: Implications for petrochronology. *Journal of Petrology*, *58*, 1031–1057.
- Garber, J. M., Smye, A. J., Feineman, M. D., Kylander-Clark, A. R. C., & Matthews, S. (2020). Decoupling of zircon U–Pb and trace-element systematics driven by U diffusion in eclogite-facies zircon (Monviso meta-ophiolite, W. Alps). *Contributions to Mineralogy and Petrology*, *175*(6), <https://doi.org/10.1007/s00410-020-01692-2>
- Gascoyne, M. (1986). Evidence for the stability of the potential nuclear waste host, sphehene, over geological time, from uranium-lead ages and uranium-series measurements. *Applied Geochemistry*, *1*(2), 199–210.
- Gerbi, C., & West, D. P. Jr. (2007). Use of U–Pb geochronology to identify successive, spatially overlapping tectonic episodes during Silurian-Devonian orogenesis in south-central Maine, USA. *Geological Society of America Bulletin*, *119*, 1218–1231.
- Ghent, E. D., & Stout, M. Z. (1984). TiO<sub>2</sub> activity in metamorphosed pelitic and basic rocks: Principles and applications to metamorphism in southeastern Canadian Cordillera. *Contributions to Mineralogy and Petrology*, *86*, 248–255.
- Gibson, D., Barr, S. M., van Rooyen, D., White, C., & Pilote, J.-L. (2021). Protracted intra- and inter-pluton magmatism during the Acadian orogeny: Evidence from new LA-ICP-MS U–Pb zircon ages from northwestern Maine, USA. *Atlantic Geology*, *57*, 1–396.
- Gordon, S. M., Kirkland, C. L., Reddy, S. M., Blatchford, H. J., Whitney, D. L., Teyssier, C., Evans, N. J., & McDonald, B. J. (2021). Deformation-enhanced recrystallization of titanite drives decoupling between U–Pb and trace elements. *Earth and Planetary Science Letters*, *560*, 116810.
- Groppo, C., Rolfo, F., Castelli, D., & Mosca, P. (2017). Metamorphic CO<sub>2</sub> production in collisional orogens: Petrological constraints from phase diagram modeling of Himalayan, scapolite-bearing, calc-silicate rocks in the NKC(F)MASH(T)-HC system. *Journal of Petrology*, *58*, 53–83.

- Guidotti, C. V. (1970). The mineralogy and petrology of the transition from lower to upper sillimanite zone in the Oquossoc area, Maine. *Journal of Petrology*, *11*, 277–336.
- Guidotti, C. V. (1985). Metamorphic map of maine. In P. H. Osberg, A. M. Hussey II & G. M. Boone (Eds.), *Bedrock geologic map of maine*. Maine Geological Survey.
- Guidotti, C. V. (1989). Metamorphism in Maine: An overview. In R. D. Tucker & R. G. Marvinney (Eds.), *Studies in Maine Geology, Maine Geological Survey* (Vol. 3, pp. 1–19). Maine Geological Survey.
- Hartnady, M. I. H., Kirkland, C. L., Clark, C., Spaggiari, C. V., Smithies, R. H., Evans, N. J., & McDonald, B. J. (2019). Titanite dates crystallization: Slow Pb diffusion during super-solidus re-equilibration. *Journal of Metamorphic Petrology*, *37*, 823–838.
- Hawthorne, F. C., Oberti, R., Harlow, G. E., Maresch, W. V., Martin, R. F., Schumacher, J. C., & Welch, M. D. (2012). Nomenclature of the amphibole supergroup. *American Mineralogist*, *97*(11–12), 2031–2048. <https://doi.org/10.2138/am.2012.4276>
- Hayden, L. A., Watson, E. B., & Wark, D. A. (2008). A thermobarometer for sphene (titanite). *Contributions to Mineralogy and Petrology*, *155*, 529–540.
- Heaman, L., & Parrish, R. (1991). U-Pb geochronology of accessory minerals. In L. Heaman & J.N. Ludden (Eds.), *Applications of radiogenic isotope systems to problems in geology*. Short Course Handbook, (Vol. 19, pp. 59–102). Mineralogical Association of Canada.
- Hibbard, J. P., van Staal, C. R., Rankin, D., & Williams, H. (2006). *Lithotectonic Map of the Appalachian Orogen (North)* (p. 02041A). Geological Survey of Canada.
- Hillenbrand, I. W., & Williams, M. L. (2021). Paleozoic evolution of crustal thickness and elevation in the northern Appalachian orogen, USA. *Geology*, *49*, 946–951.
- Hillenbrand, I. W., Williams, M. L., Li, C., & Gao, H. (2021). Rise and fall of the Acadian altiplano: Evidence for a Paleozoic orogenic plateau in New England. *Earth and Planetary Science Letters*, *560*, 116797.
- Hodges, K. V., & Crowley, P. D. (1985). Error estimation and empirical geothermobarometry for pelitic systems. *American Mineralogist*, *70*, 702–709.
- Holdaway, M. J., Dutrow, B. L., & Hinton, R. W. (1988). Devonian and Carboniferous metamorphism in west-central Maine: The muscovite-almandine geobarometer and the staurolite problem revisited. *American Mineralogist*, *73*, 20–47.
- Holdaway, M. J., Mukhopadhyay, B., Dyar, M. D., Guidotti, C. V., & Dutrow, B. L. (1997). Garnet-biotite geothermometry revised: New Margules parameters and a natural specimen data set from Maine. *American Mineralogist*, *82*, 582–595.
- Holder, R. M., & Hacker, B. R. (2019). Fluid-driven resetting of titanite following ultrahigh-temperature metamorphism in southern Madagascar. *Chemical Geology*, *504*, 38–52.
- Holder, R. M., Hacker, B. R., Seward, G. G. E., & Kylander-Clark, A. R. C. (2019). Interpreting titanite U-Pb dates and Zr thermobarometry in high-grade rocks: Empirical constraints on elemental diffusivities of Pb, Al, Fe, Zr, Nb, and Ce. *Contributions to Mineralogy and Petrology*, *174*, 1–19.
- Horstwood, S. A., Košler, J., Gehrels, G., Jackson, S. E., McLean, N. M., Paton, C., Pearson, N. J., Sircombe, K., Sylvester, P., Vermeesch, P., Bowring, J. F., Condon, D. J., & Schoene, B. (2016). Community-derived standards for LA-ICP-MS U-(Th-)Pb geochronology—Uncertainty propagation, age interpretation and data reporting. *Geostandards and Geoanalytical Research*, *40*, 311–332.
- Hubbard, M. S., West, D. P. Jr., Ludman, A., Guidotti, C. V., & Lux, D. R. (1995). The Norumbega fault zone, Maine: A mid-to shallow-level crustal section within a transcurrent shear zone. *Atlantic Geology*, *31*, 109–116.
- Hussey, A. M. (1983). Bedrock geology of the Lewiston 15-minute quadrangle, Maine. *Maine Geological Survey Open-File Report, OF-83-4*, 1–15.
- Jochum, K.P., Weis, U., Stoll, B., Kuzmin, D., Yang, Q., Raczek, I., Jacob, D.E., Stracke, A., Birbaum, K., Frick, D.A., Günther, D., Enzweiler, J. (2011). Determination of reference values for NIST SRM 610-617 glasses following ISO guidelines. *Geostandards and Geoanalytical Research*, *35*, 397–429.
- Jochum, K. P., Wilson, S. A., Abouchami, W., Amini, M., Chmeleff, J., Eisenhauer, A., Hegner, E., Iaccheri, L. M., Kieffer, B., Krause, J., McDonough, W. F., Mertz-Kraus, R., Raczek, I., Rudnick, R. L., Scholz, D. K., Steinhöfel, G., Stoll, B., Stracke, A., Tonerini, S., ... Woodhead, J. D. (2011). GSD-1G and MPI-DING reference glasses for in situ and bulk isotopic determination. *Geostandards and Geoanalytical Research*, *35*, 193–226.
- Johnson, T. E., Brown, M., & Solar, G. S. (2003). Low-pressure sub-solidus and suprasolidus phase equilibria in the MnNCKFMASH system: Constraints on conditions of regional metamorphism in western Maine, northern Appalachians. *American Mineralogist*, *88*, 624–638.
- Johnson, T. A., Cottle, J. M., & Larson, K. P. (2020). Delineation of multiple metamorphic events in the Himalayan Kathmandu Complex, central Nepal. *Journal of Metamorphic Geology*, *00*, 1–30.
- Joint Committee for Guides in Metrology. (2012). International vocabulary of metrology: Basic and general concepts (VIM). *International Bureau of Weights and Measures*, *200*, 90–95.
- Kapp, P., Manning, C. E., & Tropper, P. (2009). Phase-equilibrium constraints on titanite and rutile activities in mafic epidote amphibolites and geobarometry using titanite-rutile equilibria. *Journal of Metamorphic Geology*, *27*, 509–521.
- Kirkland, C. L., Fougereuse, D., Reddy, S. M., Hollis, J., & Saxey, D. W. (2018). Assessing the mechanisms of common Pb incorporation into titanite. *Chemical Geology*, *483*, 558–566.
- Kirkland, C. L., Hollis, J., Danišik, M., Petersen, J., Evans, N. J., & McDonald, B. J. (2017). Apatite and titanite from the Karrat Group, Greenland: Implications for charting the thermal evolution of crust from the U-Pb geochronology of common Pb bearing phases. *Precambrian Research*, *300*, 107–120.
- Kirkland, C. L., Spaggiari, C. V., Johnson, T. E., Smithies, R. H., Danišik, M., Evans, N., Wingate, M. T. D., Clark, C., Spencer, C., Mikucki, E., & McDonald, B. J. (2016). Grain size matters: Implications for element and isotopic mobility in titanite. *Precambrian Research*, *278*, 283–302.
- Kohn, M. J. (2017). Titanite petrochronology. *Reviews in Mineralogy & Geochemistry*, *83*, 419–441.
- Kohn, M. J., & Corrie, S. L. (2011). Preserved Zr-temperatures and U-Pb ages in high-grade metamorphic titanite: Evidence for a

- static hot channel in the Himalayan orogen. *Earth and Planetary Science Letters*, 311, 136–143.
- Konrad-Schmolke, M., Halama, R., Wirth, R., Thomen, A., Klitscher, N., Morales, L., Schreiber, A., & Wilke, F. D. H. (2018). Mineral dissolution and reprecipitation mediate by an amorphous phase. *Nature Communications*, 9(1637), 1–9.
- Lanari, P., Vho, A., Bovay, T., Airaghi, L., & Centrella, S. (2018). Quantitative compositional mapping of mineral phases by electron probe micro-analyser. *Geological Society of London, Special Publications*, 478, 39–63.
- Lanari, P., Vidal, O., de Andrade, V., Dubacq, B., Lewin, E., Grosch, E. G., & Schwartz, S. (2014). XMapTools: A MATLAB®-based program for electron microprobe X-ray image processing and geothermobarometry. *Computers & Geosciences*, 62, 227–240.
- Ludman, A. (1998). Evolution of a transcurrent fault system in shallow crustal metasedimentary rocks: The Norumbega fault zone, eastern Maine. *Journal of Structural Geology*, 20, 93–107.
- Ludwig, K. R. (1998). ISOPLOT for MS-DOS, a plotting and regression program for radiogenic isotope data for IBM-PC compatible computers, Version 1.00. US Geological Survey Open-File Report, OF-88-0557.
- Lux, D. R., & Guidotti, C. V. (1985). Evidence for extensive Hercynian metamorphism in western Maine. *Geology*, 13, 695–700.
- Marsh, J. H., & Smye, A. J. (2017). U-Pb systematics and trace element characteristics in titanite from a high-pressure mafic granulite. *Chemical Geology*, 466, 403–416.
- Mattinson, J. M. (1978). Age, origin, and thermal histories of some plutonic rocks from the Salinian block of California. *Contributions to Mineralogy and Petrology*, 67, 233–245.
- Mazdab, F. K. (2009). Characterization of flux-grown trace-element-doped titanite using high-mass-resolution ion microprobe (SHRIMP-RG). *Canadian Mineralogist*, 47, 813–831.
- Mezger, K., Essene, E. J., van der Pluijm, B. A., & Halliday, A. N. (1993). U-Pb geochronology of the Grenville Orogen of Ontario and New York: Constraints on ancient crustal tectonics. *Contributions to Mineralogy and Petrology*, 114, 13–26.
- Mezger, K., Rawnsley, C. M., Bohlen, S. R., & Hanson, G. N. (1991). U-Pb garnet, sphene, monazite, and rutile ages: Implications for the duration of high-grade metamorphism and cooling histories, Adirondack Mts, New York. *Journal of Geology*, 99, 415–428.
- Moecher, D. P., McCulla, J. K., & Massey, M. A. (2021). Zircon and monazite geochronology in the Palmer zone of transpression, south-central New England, USA: Constraints on timing of deformation, high-grade metamorphism, and lithospheric foundering during late Paleozoic oblique collision in the Northern Appalachian orogen. *GSA Bulletin*, 133(5–6), 1021–1038. <https://doi.org/10.1130/b35744.1>
- Papapavlou, K., Darling, J. R., Moser, D. E., Barker, I. R., EIMF, White, L. F., Lightfoot, P. C., Storey, C. D., & Dunlop, J. (2018). U-Pb isotopic dating of titanite microstructures: Potential implications for the chronology and identification of large impact structures. *Contributions to Mineralogy and Petrology*, 173, 1–15.
- Papapavlou, K., Darling, J. R., Storey, C. D., Lightfoot, P. C., Moser, D. E., & Lasalle, S. (2017). Dating shear zones with plastically deformed titanite: New insights into the orogenic evolution of the Sudbury impact structure (Ontario, Canada). *Precambrian Research*, 291, 220–235.
- Paton, C., Hellstrom, J., Paul, B., Woodhead, J., & Hergt, J. (2011). Iolite: Freeware for the visualisation and processing of mass spectrometric data. *Journal of Analytical Atomic Spectrometry*, 26(12), 2508–2518. <https://doi.org/10.1039/c1ja10172b>
- Paul, B., Paton, C., Norris, A., Woodhead, J., Hellstrom, J., Hergt, J., & Greig, A. (2012). Cell space: A module for creating spatially registered laser ablation images within the Iolite free-wear environment. *Journal of Analytical and Atomic Spectrometry*, 27, 700–706.
- Putnis, A. (2009). Mineral replacement reactions. *Reviews in Mineralogy and Geochemistry*, 70, 87–124.
- Pyle, J. M., Spear, F. S., Cheney, J. T., & Layne, G. (2005). Monazite ages in the Chesham Pond Nappe, SW New Hampshire, U.S.A.: Implications for assembly of central New England thrust sheets. *American Mineralogist*, 90, 592–606.
- Raimondo, T., Payne, J., Wade, B., Lanari, P., Clark, C., & Hand, M. (2017). Trace element mapping by LA-ICP-MS: Assessing geochemical mobility in garnet. *Contributions to Mineralogy and Petrology*, 172, 1–22.
- Rankin, D. W., Coish, R. A., Tucker, R. D., Peng, Z. X., Wilson, S. A., & Rouff, A. A. (2007). Silurian extension in the upper Connecticut Valley, United States and the origin of middle Paleozoic basins in the Québec embayment. *American Journal of Science*, 307, 216–264.
- Rapa, G., Groppo, C., Rolfo, F., Petrelli, M., Mosca, P., & Perugini, D. (2017). Titanite-bearing calc-silicate rocks constrain timing, duration and magnitude of metamorphic CO<sub>2</sub> degassing in the Himalayan belt. *Lithos*, 292–293, 364–378.
- Robinson, P., Tucker, R. D., Bradley, D., Berry, H. N., & Osberg, P. H. (1998). Paleozoic orogens in New England, USA. *GFF*, 120, 119–148.
- Romer, R. L. (2001). Lead incorporation during crystal growth and the misinterpretation of geochronological data from low-<sup>238</sup>U/<sup>204</sup>Pb metamorphic minerals. *Terra Nova*, 13, 258–263.
- Romer, R. L., & Rötzler, J. (2001). P-T-t evolution of ultrahigh-temperature granulites from the Saxon granulite massif, Germany, part II: Geochronology. *Journal of Petrology*, 42, 2015–2032.
- Romer, R. L., & Rötzler, J. (2003). Effect of metamorphic reaction history on the U-Pb dating of titanite. *Geological Society of London, Special Publications*, 220, 147–158.
- Romer, R. L., & Rötzler, J. (2011). The role of element distribution for the isotopic dating of metamorphic minerals. *European Journal of Mineralogy*, 23, 17–33.
- Romer, R. L., & Siegesmund, S. (2003). Why allanite may swindle about its true age? *Contributions to Mineralogy and Petrology*, 146, 297–307.
- Ruiz-Agudo, E., Putnis, C. V., & Putnis, A. (2014). Coupled dissolution and precipitation at mineral-fluid interfaces. *Chemical Geology*, 383, 132–146.
- Sanislav, I. V. (2011). A long-lived metamorphic history in the contact aureole of the Mooselookmeguntic pluton revealed by in situ dating of monazite grains preserved as inclusions in staurolite porphyroblasts. *Journal of Metamorphic Geology*, 29, 251–273.

- Schoene, B., & Bowring, S. A. (2006). U-Pb systematics of the McClure Mountain syenite: Thermochronological constraints on the age of the  $^{40}\text{Ar}/^{39}\text{Ar}$  standard MMhb. *Contributions to Mineralogy and Petrology*, *151*, 615–630.
- Scott, D. J., & St-Onge, M. R. (1995). Constraints on Pb closure temperature in titanite based on rocks from the Ungava Orogen, Canada: Implications for U-Pb geochronology and PTt path determinations. *Geology*, *23*, 1123–1126.
- Seydoux-Guillaume, A. M., Goncalves, P., Wirth, R., & Deutsch, A. (2003). Transmission electron microscope study of polyphase and discordant monazites: Site-specific specimen preparation using the focused ion beam technique. *Geology*, *31*, 973–976.
- Smith, H. A., & Barreiro, B. (1990). Monazite U-Pb dating of staurolite grade metamorphism in pelitic schists. *Contributions to Mineralogy and Petrology*, *105*, 602–615.
- Smith, M. P., Storey, C. D., Jeffries, T. E., & Ryan, C. (2009). In situ U-Pb and trace element analysis of accessory minerals in the Kiruna District, Norrbotten, Sweden: New constraints on the timing and orogen of mineralization. *Journal of Petrology*, *50*, 2063–2094.
- Smye, A. J., Marsh, J. H., Vermeesch, P., Garber, J. M., & Stockli, D. F. (2018). Applications and limitations of U-Pb thermochronology to middle and lower crustal thermal histories. *Chemical Geology*, *494*, 1–18.
- Solar, G. S., & Brown, M. (1999). The classic high-T–Low-P metamorphism of west-central Maine: Is it post-tectonic or syn-tectonic? Evidence from porphyroblast-matrix relations. *Canadian Mineralogist*, *37*, 311–333.
- Solar, G. S., Pressley, R. A., Brown, M., & Tucker, R. D. (1998). Granite ascent in convergent orogenic belts: Testing a model. *Geology*, *26*, 711–714.
- Solar, G. S., & Tomascak, P. B. (2016). The migmatite-granite complex of southern Maine: Its structure, petrology, geochemistry, geochronology, and relation to the Sebago Pluton. In H. N. Berry & D. P. West, Jr. (Eds.), *Guidebook for Field Trips Along the Maine Coast From Maquoit Bay to Muscongus Bay. 2016 New England Intercollegiate Geological Conference* (pp. 19–42). New England Intercollegiate Geological Conference.
- Spandler, C., Hammerli, J., Sha, P., Hilbert-Wolft, H., Hu, Y., Roberts, E., & Schmitz, M. (2016). MKED1: A new titanite standard for in situ analyses of Sm-Nd isotopes and U-Pb geochronology. *Chemical Geology*, *425*, 110–126.
- Spear, F. S., & Parish, R. R. (1996). Petrology and cooling rates of the Valhalla Complex, British Columbia, Canada. *Journal of Petrology*, *37*, 733–765.
- Spencer, K. J., Hacker, B. R., Kylander-Clark, A. R. C., Andersen, T. B., Cottle, J. M., Stearns, M. A., Poletti, J. E., & Seward, G. G. E. (2013). Campaign-style titanite U-Pb dating by laser-ablation ICP: Implications for crustal flow, phase transformations and titanite closure. *Chemical Geology*, *341*, 84–101.
- van Staal, C. R., Whalen, J. B., Valverde-Vaquero, P., Zagorevski, A., & Rogers, N. (2009). Pre-carboniferous, episodic accretion-related, orogenesis along the Laurentian margin of the northern Appalachians. *Geological Society of London, Special Publications*, *327*, 271–316.
- Stacey, J. S., & Kramers, J. D. (1975). Approximation of terrestrial lead isotope evolution by a two-stage model. *Earth and Planetary Science Letters*, *26*, 207–221.
- Stearns, M. A., Cottle, J. M., Hacker, B. R., & Kylander-Clark, A. R. C. (2016). Extracting thermal histories from the near-rim zoning in titanite using coupled U-Pb and trace element depth profiles by single-shot laser-ablation split stream (SS-LASS) ICP-MS. *Chemical Geology*, *422*, 13–24.
- Stearns, M. A., Hacker, B. R., Ratschbacher, L., Rutte, D., & Kylander-Clark, A. R. C. (2015). Titanite petrochronology of the Pamir gneiss domes: Implications for mid-deep crust exhumation and titanite closure to Pb and Zr diffusion. *Tectonics*, *34*, 1–19.
- Storey, C. D., Jeffries, T. E., & Smith, M. (2006). Common lead-corrected laser ablation ICP-MS U-Pb systematics and geochronology of titanite. *Chemical Geology*, *227*, 37–52.
- Storey, C. D., Smith, M. P., & Jeffries, T. E. (2007). In situ LA-ICP-MS U-Pb dating of metavolcanics of Norrbotten, Sweden: Records of extended geological histories in complex titanite grains. *Chemical Geology*, *240*, 163–181.
- Sun, S. S., & McDonough, W. F. (1989). Chemical and isotopic systematics of oceanic basalts: Implications for mantle composition and processes. *Geological Society of London, Special Publications*, *42*, 313–345.
- Timms, N. E., Kirkland, C. L., Cavosie, A. J., Rae, A. S. P., Rickard, W. D. A., Evans, N. J., Erickson, T. M., Wittmann, A., Ferrière, L., Collins, G. S., & Gulick, S. P. S. (2020). Shocked titanite records Chicxulub hydrothermal alteration and impact age. *Geochimica et Cosmochimica Acta*, *281*, 12–30. <https://doi.org/10.1016/j.gca.2020.04.031>
- Thomas, J. B., Watson, E. B., Spear, F. S., Shemella, P. T., Nayak, S. K., & Lanzirotti, A. (2010). Titanite under pressure: The effect of pressure and temperature on the solubility of Ti in quartz. *Contributions to Mineralogy and Petrology*, *160*, 743–759.
- Thomson, J. A., & Guidotti, C. V. (1989). Carboniferous Barrovian metamorphism in southern Maine. *Studies in Maine Geology*, *3*, 35–51.
- Tomascak, P. B., Krogstad, E. J., & Walker, R. J. (1996). U-Pb monazite geochronology of granitic rocks from Maine: Implications for late Paleozoic tectonics in the northern Appalachians. *Journal of Geology*, *104*, 185–195.
- Tomascak, P. B., & Solar, G. S. (2016). Anatomy of the migmatite-granite complex, Southwestern Maine. Geological Society of America, Northeastern section, abstracts with programs, 48.
- Tucker, R. D., Råheim, A., Krogh, T. E., & Corfu, F. (1987). Uranium-lead zircon and titanite ages from the northern portion of the Western Gneiss Region, south-central Norway. *Earth and Planetary Science Letters*, *81*, 203–211.
- Tucker, R. D., Robinson, P., Solli, A., Gee, D. G., Thorsnes, T., Krogh, T. E., Nordgulen, O., & Bickford, M. E. (2004). Thrusting and Extension in the Scandian Hinterland, Norway: New U-Pb Ages and Tectonostratigraphic Evidence. *American Journal of Science*, *304*(6), 477–532. <https://doi.org/10.2475/ajs.304.6.477>
- van Malderen, S. J. M., van Elteren, J. T., Šelih, V. S., & Vanhaecke, F. (2018). Considerations on data acquisition in laser ablation-inductively coupled plasma-mass spectrometry with low-dispersion interfaces. *Spectrochimica Acta Part B Atomic Spectroscopy*, *140*, 29–34.
- Vermeesch, P. (2018). IsoplotR: A free and open toolbox for geochronology. *Geoscience Frontiers*, *9*, 1479–1493.

- Verts, L. A., Chamberlain, K. R., & Frost, C. D. (1996). U-Pb sphene dating of metamorphism: The importance of sphene growth in the contact aureole of the Red Mountain pluton, Laramie Mountains, Wyoming. *Contributions to Mineralogy and Petrology*, 125, 186–199.
- Walters, J. B., & Kohn, M. J. (2017). Protracted thrusting followed by late rapid cooling of the Greater Himalayan Sequence, Annapurna Himalaya, Central Nepal: Insights from titanite petrochronology. *Journal of Metamorphic Geology*, 35, 897–917.
- Weinberg, R. F., Wolfram, L. C., Nebel, O., Hasalová, P., Závada, P., Kylander-Clark, A. R. C., & Becchio, R. (2020). Decoupled U-Pb date and chemical zonation of monazite in migmatites: The case for disturbance of isotopic systematics by coupled dissolution-reprecipitation. *Geochimica et Cosmochimica Acta*, 269, 398–412.
- West, D. P. Jr. (1999). Timing of displacements along the Norumbega fault system, south-central and south-coastal Maine. In A. Ludman & D. P. West, Jr. (Eds.), *Norumbega Fault System of the Northern Appalachians* (Vol. 331, pp. 167–178). Geological Society of American Special Paper.
- West, D. P. Jr., & Hubbard, M. S. (1997). Progressive localization of deformation during exhumation of a major strike-slip shear zone: Norumbega fault zone, south-Central Maine, USA. *Tectonophysics*, 273, 185–201.
- Whitney, D. L., & Evans, B. W. (2010). Abbreviations for names of rock-forming minerals. *American Mineralogist*, 95, 185–187.
- Wing, B. A., Ferry, J. M., & Harrison, T. M. (2003). Prograde destruction and formation of monazite and allanite during contact and regional metamorphism of pelites: Petrology and geochronology. *Contributions to Mineralogy and Petrology*, 145, 228–250.
- Woodhead, J. D., Hellstrom, J., Hergt, J. M., Greig, A., & Maas, R. (2007). Isotopic and elemental imaging of geological materials by laser ablation inductively coupled plasma-mass spectrometry. *Geostandards and Geoanalytical Research*, 31, 331–343.

## SUPPORTING INFORMATION

Additional supporting information may be found in the online version of the article at the publisher's website.

**Table S1.** Major and minor element compositions measured by EPMA.

**Table S2.** Titanite U–Pb data, trace element, and Zr-in-titanite thermometry data.

**Table S3.** Analytical conditions,  $^{207}\text{Pb}/^{206}\text{Pb}$  of U-poor phases, and reproducibility of secondary reference materials.

**Table S4.** LA-ICP-MS trace element data of major minerals.

**Data S1.** Supplemental Text and figures.

**How to cite this article:** Walters, J. B., Cruz-Uribe, A. M., Song, W. J., Gerbi, C., & Biela, K. (2022). Strengths and limitations of in situ U–Pb titanite petrochronology in polymetamorphic rocks: An example from western Maine, USA. *Journal of Metamorphic Geology*, 40(6), 1043–1066. <https://doi.org/10.1111/jmg.12657>